# Supernova host galaxies in the dark energy survey: I. Deep coadds, photometry, and stellar masses

P. Wiseman [1]★ M. Smith,[1] M. Childress [1] L. Kelsey [1] A. Möller,[2] R. R. Gupta,[3]
E. Swann,[4] C. R. Angus [1,5] D. Brout,[6]† T. M. Davis [7] R. J. Foley,[8] C. Frohmaier,[4]
L. Galbany,[9] C. P. Gutiérrez,[1] C. Inserra,[1,10] R. Kessler,[11,12] G. F. Lewis,[13] C. Lidman,[14]
E. Macaulay,[4] R. C. Nichol,[4] M. Pursiainen,[1] M. Sako,[6] D. Scolnic [15]
N. E. Sommer,[14] M. Sullivan,[1] B. E. Tucker,[14] T. M. C. Abbott,[16] M. Aguena,[17,18]
S. Allam,[19] S. Avila,[20] E. Bertin,[21,22] D. Brooks,[23] E. Buckley-Geer,[19] D. L. Burke,[24,25]
A. Carnero Rosell,[26] D. Carollo,[27] M. Carrasco Kind,[28,29] L. N. da Costa,[18,30]
J. De Vicente,[26] S. Desai,[31] H. T. Diehl,[19] P. Doel,[23] T. F. Eifler,[32,33] S. Everett,[8]
P. Fosalba,[34,35] J. Frieman,[12,19] J. García-Bellido,[20] E. Gaztanaga,[34,35]
D. W. Gerdes,[36,37] M. S. S. Gill,[25] K. Glazebrook,[38] R. A. Gruendl,[28,29]
J. Gschwend,[18,30] W. G. Hartley,[23,39,40] S. R. Hinton,[7] D. L. Hollowood,[8]
K. Honscheid,[41,42] D. J. James,[43] K. Kuehn,[44,45] N. Kuropatkin,[19] M. Lima,[17,18]
M. A. G. Maia,[18,30] M. March,[6] P. Martini,[41,46] P. Melchior,[47] F. Menanteau,[28,29]
R. Miquel,[48,49] R. L. C. Ogando,[18,30] F. Paz-Chinchón,[29,50] A. A. Plazas,[47]
A. K. Romer,[51] A. Roodman,[24,25] E. Sanchez,[26] V. Scarpine,[19] S. Serrano,[34,35]
E. Suchyta,[52] M. E. C. Swanson,[29] G. Tarle,[37] D. Thomas,[4] D. L. Tucker,[19]
T. N. Varga,[53,54] A. R. Walker,[16] and R. D. Wilkinson[51] (DES Collaboration)

*Affiliations are listed at the end of the paper*

## ABSTRACT

The 5-yr Dark Energy Survey Supernova Programme (DES-SN) is one of the largest and deepest transient surveys to date in terms of volume and number of supernovae. Identifying and characterizing the host galaxies of transients plays a key role in their classification, the study of their formation mechanisms, and the cosmological analyses. To derive accurate host galaxy properties, we create depth-optimized coadds using single-epoch DES-SN images that are selected based on sky and atmospheric conditions. For each of the five DES-SN seasons, a separate coadd is made from the other four seasons such that each SN has a corresponding deep coadd with no contaminating SN emission. The coadds reach limiting magnitudes of order $\sim$27 in $g$ band, and have a much smaller magnitude uncertainty than the previous DES-SN host templates, particularly for faint objects. We present the resulting multiband photometry of host galaxies for samples of spectroscopically confirmed type Ia (SNe Ia), core-collapse (CCSNe), and superluminous (SLSNe) as well as rapidly evolving transients (RETs) discovered by DES-SN. We derive host galaxy stellar masses and probabilistically compare stellar-mass distributions to samples from other surveys. We find that the DES spectroscopically confirmed sample of SNe Ia selects preferentially fewer high-mass hosts at high-redshift compared to other surveys, while at low redshift the distributions are consistent. DES CCSNe and SLSNe

★ E-mail: P.S.Wiseman@soton.ac.uk
† NASA Einstein Fellow.

hosts are similar to other samples, while RET hosts are unlike the hosts of any other transients, although these differences have not been disentangled from selection effects.

**Key words:** techniques: image processing – catalogues – supernovae: general.

# 1 INTRODUCTION

The accelerating expansion of the Universe, hypothesized to be driven by an unknown dark energy, is one of the largest unsolved problems in physics, astronomy, and cosmology. The discoverers used type Ia supernovae (SNe Ia) as standardizable candles to measure distances across the cosmos (Riess et al. 1998; Perlmutter et al. 1999). Since then, the scale of sky surveys dedicated to improving upon the accuracy and precision of cosmological measurements has increased dramatically (e.g. Astier et al. 2006; Kessler et al. 2009; Conley et al. 2011; Suzuki et al. 2012; Betoule et al. 2014). The Pantheon analysis (Scolnic et al. 2018) included a sample of >1000 SNe Ia, and when combined with the cosmic microwave background (CMB) constraints from Planck Collaboration (2016) measured the dark energy equation-of-state parameter $w$ to a precision of ~0.04. The Dark Energy Survey Supernova Programme (DES-SN) is in the process of building an even larger sample and is aiming to further reduce systematic uncertainties. The results from the first 3 yr of the survey (DES3YR) have recently demonstrated the state-of-the-art precision capabilities of DES-SN (DES Collaboration 2018). The DES3YR analysis included a photometric pipeline to determine light curves of 207 SNe Ia (Brout et al. 2019a), spectroscopy using a range of large telescopes (D'Andrea et al. 2018), a comprehensive analysis of the systematic uncertainties (Brout et al. 2019b), a suite of simulations (Kessler et al. 2019), inclusion of chromatic corrections to the calibration (Lasker et al. 2019), and a measurement of the Hubble constant, $H_0$ (Macaulay et al. 2019).

SNe Ia cosmology has traditionally been performed with 'spectroscopic samples', in which all SNe in the sample have been confirmed as SNe Ia by analysing a spectrum of the SN. As transient surveys probe larger areas with deeper observations, however, it not feasible to classify all of the SNe spectroscopically. We thus define samples by classifying SNe 'photometrically', principally using the light-curve shape and colour to distinguish SNe Ia from core-collapse events using classifiers such as pSNid (Sako et al. 2008), SuperNNova (Möller & de Boissière 2019), and RAPID (Muthukrishna et al. 2019).

In both spectroscopic and photometric samples, determination of the host galaxy associated with each SN is crucial. First, narrow emission and/or absorption lines in the spectrum of a host galaxy provide a much more precise measurement of the redshift than the broader lines of the SN spectrum, allowing for smaller uncertainties on the redshift axis of the Hubble diagram. Redshifts from the hosts improve the photometric classification of transients (e.g. Olmstead et al. 2014; Sako et al. 2014), with classification accuracy of the SuperNNova classifier improving from 97 per cent to >99 per cent with the addition of redshift (Möller & de Boissière 2019). Secondly, even after brightness corrections are applied using known correlations in their light-curve shape (stretch) and colour, a residual intrinsic scatter in their absolute peak brightness is still measured. There exist further correlations, between the properties of the SN host galaxy and the colour-and-stretch corrected brightness (or Hubble residual) of the SN (e.g. Sullivan et al. 2006; Rigault et al. 2013; Roman et al. 2018). Of these, stellar mass is the most robust and easily measured, leading to the so-called mass step correction (e.g. Kelly et al. 2010; Lampeitl et al. 2010; Sullivan et al. 2010;

Conley et al. 2011; Childress, Wolf & Zahid 2014). Understanding the driver behind, and correcting for, the mass step is the focus of significant ongoing work (Jones et al. 2018; Rigault et al. 2018; Roman et al. 2018; Rose, Garnavich & Berg 2019; Smith et al. 2020; Kelsey in preparation), all of which requires accurate and precise galaxy photometry.

Host galaxy properties are important not only for cosmological measurements but also in the quest to understand the SN explosions themselves. Most commonly used due to their observational ease and simplicity, particularly at higher redshift, are global host galaxy properties. These include stellar mass, age, and star-formation rate (SFR), and are derived from observations of the galaxy as a whole. For nearby, spatially resolved galaxies, especially those for which integral field spectroscopy (IFS) observations are available, local properties can provide an extra channel from which to inform the host study (e.g. Thöne et al. 2014; Krühler et al. 2017a; Galbany et al. 2018; Schady et al. 2019). Local properties are typically analogues of the global properties, but are derived from a region smaller than the entire host galaxy, and are used to provide a more accurate representation of the properties of the particular stellar population from which the progenitor was born (e.g. Rigault et al. 2013; Roman et al. 2018).

Galaxy properties are commonly used to infer the nature of transients. Events linked to massive stars tend to occur in star-forming galaxies, thermonuclear transients, and compact object mergers occur more universally (e.g. Childress et al. 2013a; Palmese et al. 2017), and tidal disruption events (TDEs) often occur in post-starburst E+A galaxies (Arcavi et al. 2014; French, Arcavi & Zabludoff 2016; Krühler et al. 2017b). More specifically, the myriad subclasses of SNe each show a preference towards certain host properties: among those associated with massive stars, the most energetic such as gamma-ray bursts (GRBs; e.g. Fruchter et al. 2006; Perley et al. 2016b; Graham & Fruchter 2017), superluminous supernovae (SLSNe; e.g. Neill et al. 2011; Angus et al. 2016; Chen et al. 2017a), and relativistic broad-line SNe (Ic-bl; Japelj et al. 2018; Modjaz et al. 2020) typically occur in environments low in metallicity and stellar mass, and/or high in specific star formation rate (sSFR; SFR per unit stellar mass), while more typical core collapse SNe (CCSNe) are more agnostic (e.g. Anderson et al. 2010). The relatively small numbers of objects in some of these samples mean selection effects are also at play and must be correctly accounted for when drawing conclusions about progenitor populations.

Host galaxy properties can be estimated from photometry, slit spectroscopy, and more recently IFS. While spectroscopy is able to provide more detailed information about the physical processes at play in the galaxies, it is expensive and time-consuming. The magnitude limits of spectroscopy are relatively shallow, which is a limitation when dealing with SNe at high redshifts or in faint host galaxies. On the other hand, the nature of wide-field, untargeted searches such as DES means that there is by design a wealth of imaging of the host for each and every transient detected in the survey in the form of the single-epoch exposures. In order to detect transients, a template image is subtracted from each single epoch exposure in a technique known as difference imaging. During the DES science verification (SV; see Bonnett et al. 2016; Jarvis et al. 2016; Rykoff et al. 2016 for a detailed description of the

SV data[1]), templates for difference imaging (Kessler et al. 2015) were constructed from roughly three nights of observing. While the difference imaging templates were updated throughout the survey with data from each season, the original SV templates (via the SVA1_GOLD catalogue) were used to determine host galaxy properties for spectroscopic target selection (D'Andrea et al. 2018) and in the cosmology analysis (Brout et al. 2019b). In this work, we improve upon those templates by building coadds from the full survey.

The main DES-SN survey consisted of five annual, six-month observing seasons with repeated, roughly 7-d cadence observations in each of 10 pointings of the 2.7 deg$^2$ field-of-view Dark Energy Camera (DECam; Flaugher et al. 2015), denoted the SN fields (Section 2.2). With a total of ~120 visits to each field by the end of the survey (Diehl et al. 2016, 2018), it is possible to improve upon the SV templates by stacking single-epoch images into coadds. Such a method has been used in other repeat-observation surveys such as SDSS Stripe 82 (Annis et al. 2014). In building a deep host galaxy template for each SN, it is necessary to omit the epochs in which the SN is active. Typically, this is done by building separate multiseason coadds, omitting each season in turn (e.g. Pan-STARRS; Rest et al. 2014; Scolnic et al. 2018). SNe fade by several orders of magnitude on the time-scale of a year – SN2003hv was around 7 mag fainter than at peak in all optical bands 300-d post-peak (Leloudas et al. 2009), while the equivalent decline for SN2012fr to 150 d was 5 mag (Contreras et al. 2018). Thus for 'normal' SNe Ia occurring at the end of a season, their contribution to the host galaxy flux in the subsequent season beginning ~6 months later is negligible. For SLSNe, whose light-curve durations often exceed that of a DES observing season, it can be necessary to exclude data from the subsequent season and as such these coadds may not be suitable for analysing the hosts of some of the SLSNe in DES-SN.

In this paper, we lay the foundations for the analysis of the host galaxies of the full DES-SN data set. We build a suite of depth-optimized coadds and perform diagnostic tests comparing these coadds to other catalogues, which is described in Section 2. In Section 3, we analyse the host galaxies of various transients in DES-SN, focusing on fitting their spectral energy distributions (SEDs) with stellar population templates. In Section 4, we describe the results of the SED fitting and report host masses for various subsets of transients. We summarize with a discussion and conclusion in Sections 5 and 6, respectively. Throughout this paper, we adopt a spatially-flat ΛCDM cosmological model with a matter density $\Omega_m = 0.3$ and Hubble constant $H_0 = 70 \, \mathrm{km \, s^{-1} \, Mpc^{-1}}$. We use AB magnitudes (Oke & Gunn 1983) and report uncertainties at the $1\sigma$ level unless otherwise stated.

# 2 DEEP PHOTOMETRY

## 2.1 DES-SN survey overview

DES-SN consisted of a survey of 10 separate pointings, grouped into four regions on the sky. Each of these fields was chosen to coincide with a deep extragalactic legacy field: three overlapping with XMM-LSS (the 'SN-X' fields; Pierre et al. 2004); three with the Chandra Deep Field – South (the 'SN-C' fields; Xue et al. 2011); two overlapping with the Sloan Digital Sky Survey (SDSS) Stripe 82 (the 'SN-S' fields; Adelman-McCarthy et al. 2007; Abazajian et al. 2009); and two overlapping with the Elais-S1 field (the 'SN-E'

fields; Oliver et al. 2000). In both the X and C regions, one of the three pointings was subject to longer exposures and is thus denoted a 'deep field'. The remaining eight are referred to as 'shallow fields'. The DES photometric bands, $g$, $r$, $i$, and $z$, correspond closely to their SDSS analogues. Observations were taken in each band roughly every 7 d (although exposures failing quality cuts were repeated at the next available opportunity) over 5 yr, comprising 6-month observing seasons during consecutive southern summers. Single-visit limiting magnitudes are $m_{\mathrm{lim, \, single \, epoch}} \sim 23.5$ for shallow fields, and 24.5 for deep fields. Further description of the SN survey and spectroscopic targeting can be found in Kessler et al. (2015) and D'Andrea et al. (2018).

## 2.2 Coadds

The extensive observations obtained by DES-SN open up the possibility for the creation of deep images by coadding the individual exposures. While the deepest coadds are obtained by combining data from all five seasons, for the purposes of studying SN host galaxies it is important to remove those exposures that contain light from the SN. While it is possible to make an individual coadd for each SN using all exposures minus the exact ones for which that SN was visible, this is computationally expensive and encounters issues such as a precise knowledge of when the SN faded below the detection threshold. As such we create a series of four-season coadds, for each one excluding all exposures from the other season. We refer to such image stacks as minus-year (MY) coadds: the coadd missing season one is referred to as MY1, and so on. For SNe detected in season $S$, there is a respective coadd MY$S$ for which all exposures from season $S$ are excluded. To create the coadds, we use a custom pipeline[2] that makes extensive use of software from the ASTROMATIC[3] suite. The full set of configuration files used in coaddition and photometry can be found in the publically available github repository in footnote.[2]

### 2.2.1 Selecting exposures

The inclusion of particularly poor-quality exposures, such as those affected by instrumental noise, high seeing, or clouds, can have a detrimental effect on the quality of a coadd. Poor seeing results in the washing-out of sources in the resulting stacked image, degrading the limiting magnitude for extended sources. While theoretically all epochs with a signal-to-noise ratio greater than unity should improve the depth of the final coadd, empirical tests show that better coadd depth is achieved by introducing selection requirements (cuts), which a single exposure must pass before being included. For this purpose, we use the effective exposure time ratio $\tau$ (Neilsen et al. 2016). This is the ratio between the effective exposure time, given the conditions, $t_{\mathrm{eff}}$, and the true exposure time $t_{\mathrm{exp}}$, and is given by

$$\tau = \eta^2 \left( \frac{\mathrm{FWHM}}{0.9 \, \mathrm{arcsec}} \right)^{-2} \left( \frac{b}{b_{\mathrm{dark}}} \right)^{-1}, \tag{1}$$

where $\eta$ is the atmospheric transmission, $b$ is the sky brightness, and FWHM corresponds to the full width at half-maximum of the point spread function (PSF) on a particular night. This measure is normalized to the following set of good conditions in the $i$ band: $\eta = 1$, FWHM = 0.9 arcsec, and $b_{\mathrm{dark}}$ corresponding to the background
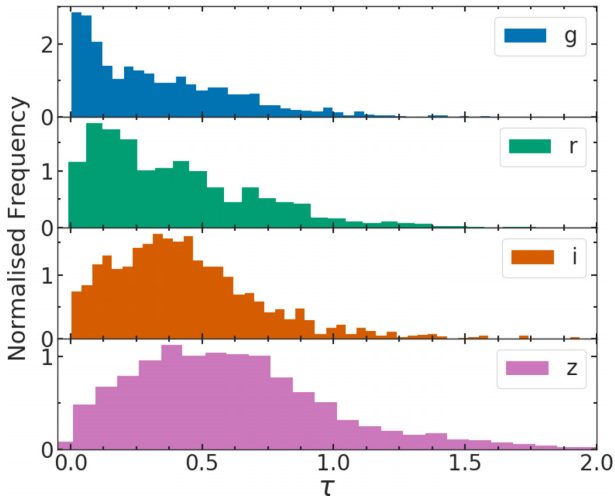
**Figure 1.** Histograms for the distribution of effective exposure time ratio $\tau$ (the ratio between the true exposure time, and the effective exposure time based on the atmospheric and sky background conditions; equation 1) across all DES-SN exposures. The distributions peak at progressively higher values at higher wavelengths, meaning that a larger fraction of the $i$ and $z$ band exposures are closer to the fiducial 'good' conditions.

from a dark sky at zenith. For more details on $\tau$ and $t_{\rm eff}$ in DES, see Morganson et al. (2018). A value of $\tau = 1$ corresponds to good conditions, while lower values mean that the effective exposure time is shorter than it would have been had the conditions been the same as the fiducial 'good' ($\tau = 1$) ones. The distribution of $\tau$ over the 5 yr of DES-SN is shown in Fig. 1. There is an evident difference in the $\tau$ distributions between filters. The median $\tau$ in $g$ is much smaller than $z$ due to the dependence of atmospheric turbulence on wavelength and the increased degradation caused by the moon at shorter wavelengths. Structure in the histograms, such as steps around $\tau \sim 0.3$, can be explained by the use of data quality thresholds to determine whether observations should be repeated at the next available opportunity (Neilsen et al. 2019). This effect can also be seen in the distribution of seeing measured in the survey in Fig. 2, which shows a higher average seeing in the $g$ and $r$ bands.

To exclude the worst exposures, a $\tau$ cut is made. Exposures for which $\tau$ is below this cut are not included in the coadd. Similarly, we make cuts on the seeing as measured in the initial reduction of the image. In order to find the values for $\tau_{\rm cut}$ and PSF that optimize the limiting magnitude of the final images, we conduct a series of test coadds. For each test, the exposures passing the corresponding cuts are coadded using the method outlined in Section 2.2.2 and the limiting magnitude is measured (c.f. Section 2.3.2) and recorded. Wider ranging $\tau$ cuts and PSF cuts were initially tested, using coarser $\tau$ steps in order to reduce CPU expense. The final optimization is then run on a smaller range of $\tau$ with finer steps. The optimization is performed independently in each band, and on a shallow (X2) and a deep (X3) field, although the choice of field does not influence the final adopted cuts.

The optimum PSF cut was found to be 2.4 arcsec ($g$) and 2.2 arcsec ($r, i, z$) for all fields. Figs 3 and 4 show the results from the $\tau$ optimization in the shallow and deep field, respectively. Positive values correspond to a deeper image (greater limiting magnitude) than the fiducial 'no cuts' coadd. In some bands, there is a clear evolution in the limiting magnitude based on different $\tau_{\rm cut}$, although this is not evident in others (e.g. $r$). In the shallow fields, the trend is most obvious in $g$ and $z$, where very lenient cuts, and thus inclusion
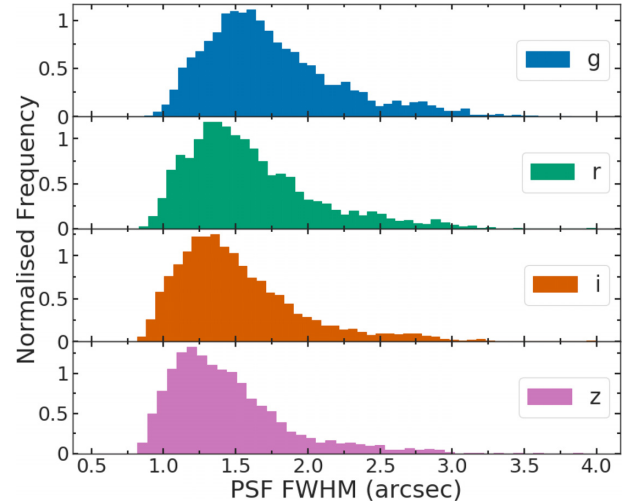


**Figure 2.** Histograms for the distribution of the PSF FWHM across all DES-SN exposures. The distributions share similar shapes with long, high-seeing tails, which are all excluded from the stacks by the seeing cut. The distributions peak at increasingly smaller values as the filter wavelength increases.
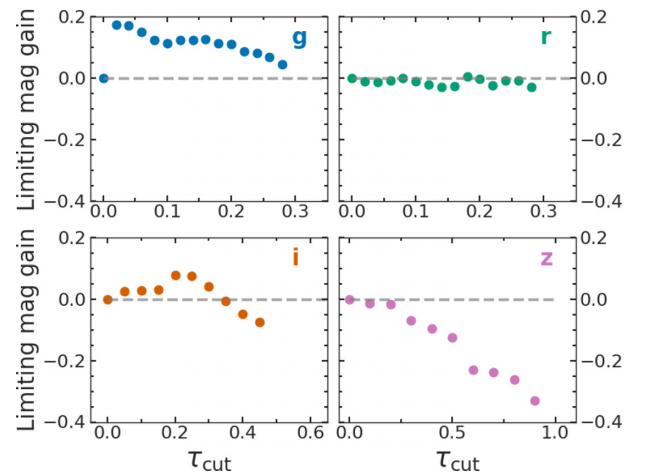


**Figure 3.** The difference in limiting magnitudes (measured from the sky background rms; explained in Section 2.3.2) of coadds of CCD 35 in the shallow X2 field, based upon different cuts in $\tau$. The higher the cut in $\tau$, the more single epochs are rejected from inclusion in the stack. The difference is measured compared to the coadd with no cuts ($\tau = 0$).

of all single epochs, result in the deepest coadds. In $r$ and $i$, on the other hand, the depth peaks at $0.2 \leq \tau_{\rm cut} \leq 0.3$. We note that for $g$, $r$, and $i$, the variation in limiting magnitude between $0 \leq \tau_{\rm cut} \leq 0.3$ is about $\pm 0.05$ dex, which is smaller than the typical statistical error on objects of such brightness, and also smaller than the rms variation seen across different CCDs and fields. For reasons related to further optimizing, the trade-off between depth and computational expense, we chose shallow field $\tau$ cuts of 0.26 in $g$, 0.2 in $r$, and $i$, and 0.3 in $z$. For the same reasons, in the deep fields we choose $\tau$ cuts of 0.06, 0.2, 0.4, and 0.5 for $g$, $r$, $i$, and $z$, respectively. We note that the $i$-band limiting magnitude increases with $\tau_{\rm cut}$ in the deep fields, whereas the other bands are relatively flat. Similarly, the variation in the deep field $\tau_{\rm cut}$ values is larger than for shallow fields. We suggest it is likely caused by the differing distributions of $\tau$ in each filter, although it is not immediately clear why this should be the
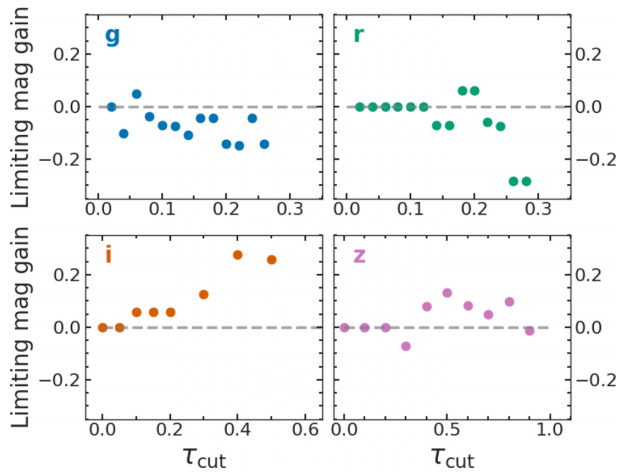
**Figure 4.** As for Fig. 3, but for CCD 35 in the deep X3 field.

case. We stress that the results presented in this and future analyses are robust to small shifts in the $\tau$ cut, as the inclusion/exclusion of single images has a negligible effect on whether a host is detected or not. A summary of the cuts for each field and band is given in Table A1.

While here we optimize the stacks for their ultimate depth, using limiting magnitude as a diagnostic, this simple method makes it possible to quickly optimize the cutting procedure for any desired output variable. For example, the analysis of Kelsey (in preparation) uses a version of these coadds that has been optimized for the best seeing in order to resolve subgalactic scale regions of SN Ia hosts to improve measurements of local properties around the SN locations.

### 2.2.2 Coaddition

Individual exposures are detrended through the Dark Energy Survey Image Processing Pipeline (Morganson et al. 2018). To stack the individual exposures, we use SWarp (Bertin et al. 2002). Each of the 59 DECam science, CCDs functioning for the entire survey duration are treated independently. For each chip, in each field, band, and MY combination, all exposures passing the relevant PSF and $\tau$ criteria are resampled using the default Lanczos-3 $6 \times 6$-tap filter, and then coadded. The resampling may affect photometric uncertainties by introducing correlations between resampled pixels. However, this effect is negligible compared to the dominant zero-point uncertainty (Section 2.3). Due to the large number of input exposures, which themselves are already deep, the commonly-used mean and weighted mean stacking methods lead to the contamination of the final coadd by a high density of artefacts such as satellite trails and cosmic rays. Median and clipped median stacks, which are efficient at removing artefacts, lead to systematic offsets in the photometry of bright objects (e.g. Gruen, Seitz & Bernstein 2014a), due to the inhomogeneity of the PSFs of the single epochs. We therefore utilize the clipped mean stacking method (Gruen et al. 2014a, and code therein[4]), whereby outlier pixels are detected by performing a clipping procedure. The detected outlier regions in individual exposures are masked, before the implementation of a weighted average stack, using inverse variance weight maps. This method has previously been implemented in several analyses (e.g. Gruen et al. 2014b; Melchior et al. 2015).

[4]https://web.stanford.edu/~dgruen/download.html

### 2.3 Photometry

#### 2.3.1 Calibration

To perform a photometric calibration on the coadds, we calculate photometric zero-points by matching stars to existing catalogues. The zero-points are then used to calibrate the common aperture photometry (CAP) described in Section 2.3.3. Sources for use in the calibration are detected using Source Extractor (Bertin & Arnouts 1996). In order to calculate zero-points for the coadd images, detected sources are matched to a catalogue made using the first 3 yr of the DES wide-area survey, known as Y3A1, via the DES Image Processing Pipeline (Morganson et al. 2018). We make use of the MODEST classifier (e.g. Chang et al. 2015) to select robustly classified stars from the catalogue, imposing the additional criterion that stars must be brighter than 22nd magnitude, where the scatter is lowest and the MODEST classifications are most robust. We exclude stars brighter than 18th magnitude, as we find that the coaddition technique leads in some cases to the clipping of the centres of the images of particularly bright stars. We calculate the magnitude zero-point and its uncertainty for each deep image by using the median of the zero-points from each individual bright star match, and the corresponding median absolute deviation (MAD) divided by the square root of the number of stars: $ZP_{err} = MAD/\sqrt{n}$. This uncertainty dominates the total photometric uncertainty, particularly for brighter objects whose statistical uncertainty is lower.

#### 2.3.2 Limiting magnitudes

There are multiple methods to calculate the limiting magnitude of an image; that is, the magnitude fainter than which limits are reported rather than detections. First, the limiting magnitude can be approximated from the distribution of the magnitudes of detected sources. The magnitude at which the distribution peaks is taken as the limiting magnitude. This is because the true magnitude distribution of sources rises to much fainter values, so the turn-off is indicating that some objects are not being detected. This method is quite strongly dependent upon the parameters used during the source extraction process such as the detection threshold chosen, since using a lower detection threshold will push the peak of the distribution to fainter magnitudes, but there is a greater chance that these detections will be false.

Secondly, a limiting magnitude can be calculated using the measurement uncertainty of the magnitudes of detected objects. The limit is simply the magnitude at which the mean magnitude error of objects, $\sigma_m$, is equal to a threshold determined by the precision required. $10\sigma$ is the typically quoted value in DES (e.g. Jarvis et al. 2016), and thus our threshold becomes $\sigma_m = 0.1$.

Thirdly, one can calculate the limiting magnitude using the rms of the background, $m_{b; rms}$, using

$$m_{lim} = m_{zp} - 2.5 \log\left(n \times m_{b;rms}\sqrt{\pi FWHM^2}\right), \qquad (2)$$

where $n$ corresponds to the sigma-level required, and $m_{zp}$ is the zero-point magnitude. For this catalogue, we report $5\sigma$ limits. The FWHM is the mean measured for the point sources in the field, in pixels. Here, we use the median FWHM of all objects in order to calculate an average object detection limit.

The distributions of limiting magnitudes measured in the above ways is shown in Fig. 5. The $5\sigma$ sky magnitude limit and stellar magnitude turnover are broadly consistent with each other for all fields. The $10\sigma$ measurement based on magnitude uncertainties is brighter, as expected, than the $5\sigma$ limit from the background.
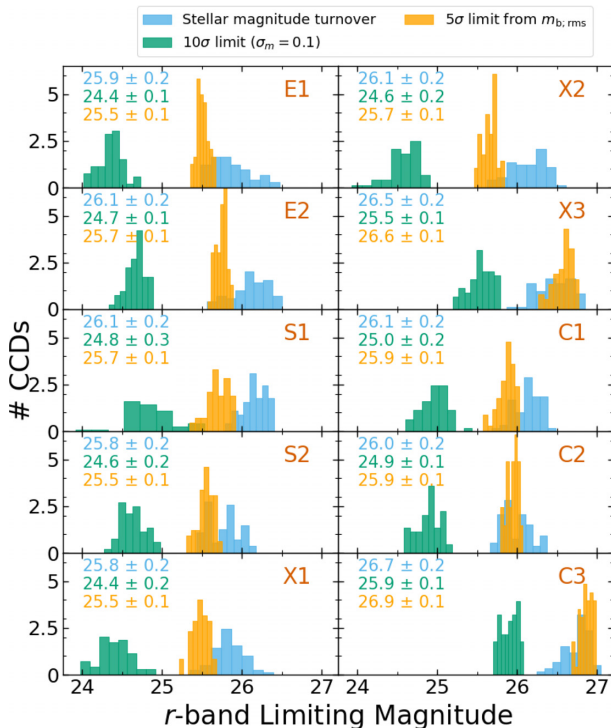
**Figure 5.** Histograms of the limiting *r*-band magnitudes for all CCDs in each of the 10 SN fields for the MY1 coadd. The extra magnitude of depth in the deeper fields, X3 and C3, is clearly evident. The means and standard deviations of the limiting magnitude distributions are displayed in the upper left corner for each field. While we report $5\sigma$ limits in this catalogue, we also show $10\sigma$ limits from magnitude uncertainties (green) for consistency with previous catalogues. Summaries of the coadd properties are given in Table A1.

The deep fields, X3 and C3, are a magnitude deeper in all three diagnostics. We note that C3 is deeper than X3, due to $\sim 30$ more epochs, corresponding to $\sim 3$ h, passing cuts (Table A1). For the assessment of depth used in Section 2.2.1, we use the sky magnitude, as it is independent of the choice of source-detection parameters. During the initial set of tests, we trialled using different measurements of depth but the effect on the chosen cuts was negligible.

### 2.3.3 Common aperture photometry

The most accurate photometry requires a model of the PSF (for point sources) as well as a morphological model with which to convolve it (for galaxies). In `Source Extractor`, these techniques correspond to the `MAG_PSF` and `MAG_MODEL` magnitudes, respectively. However, in the deep coadds, the PSF of the final image is a combination of the PSFs of the $\sim 100$ individual exposures. Such a composite PSF is non-trivial to model and as such renders those magnitude measurements unreliable, although efforts have been made to homogenize the PSF at the coadding stage (Mohr et al. 2012). Instead, as we are chiefly interested in fitting galaxy SEDs, we employ CAP in order to ensure we are detecting light from the same physical area in each band, and therefore maintaining consistent galaxy colours. For CAP, `Source Extractor` is run in dual-image mode, whereby the measurement apertures are defined on a detection image and used for the subsequent measurement in all four bands. For the detection image, we use

a simple average combination of $r + i + z$. We also trialed using $g + r + i$, $g + r + i + z$, as well as just $i$ and $z$ as detection images, and found that $r + i + z$ is most reliable at detecting faint objects. The magnitudes recovered when using different detection images are consistent within the measurement uncertainties.

One of the biggest issues encountered in source detection in deep images is the vast dynamic range of source brightnesses that we wish to measure. Galaxies in the deep fields span the magnitude range $14 \leq M_r \leq 28$. Naturally, we wish to report magnitudes that are accurate across this range, but particularly at the fainter end, where the existing catalogues we seek to improve on do not extend to. A large part of the problem in detecting and measuring faint objects is the task of deblending, where they may lie close to, or overlap with (in either a physical or projected sense) a much larger, brighter source. The detection of such objects can be achieved by tuning the detection parameters in `Source Extractor`. The parameters refer to flux threshold (compared to the background), and number of pixels above this threshold, required for a detection. We set these low at $1.25\sigma$ and 3 pixels, respectively, such that objects can be PSF-size and of low significance to count as detections. While raising the number of false detections, the number of these is small upon visual inspection. The low thresholds allow small, faint objects to be detected but they are often located close to larger brighter objects and `Source Extractor` may deem them to be part of the same object. Using `Source Extractor` default values for deblending parameters in an initial run, we compared the recovered host galaxies of DES-SNe with the corresponding hosts in SVA1. Four SN host galaxies with detections in SVA1 had not been picked up in the deep coadds, of which all were in small, faint, PSF-like sources near large, bright galaxies. We adjusted the deblending parameters[5] until these hosts were detected correctly.

We use the Kron magnitude (`MAG_AUTO`) output from `Source Extractor`, as well as circular aperture measurements with the aperture diameter set to 2 arcsec. This diameter corresponds to the width of the AAOmega fibres to allow for direct comparisons with, and calibrations of, galaxy and transient spectra taken as part of the DES-SN spectroscopic follow-up programme, OzDES (Yuan et al. 2015; Childress et al. 2017; Lidman et al. 2020).

We use the magnitude zero-points previously calculated from the good-quality stars to calibrate the CAP, resulting in the catalogue we name SN Deep.

### 2.4 Performance

A section of the SN Deep coadd is shown in Fig. 6 and is compared to the SVA1 coadd. The increased depth is evident due to the large number of extra sources detected, as well as the extent of existing objects.

The SVA1 *r*-band $10\sigma$ limiting magnitude is reported as approximately 23.8.[6] In Fig. 5, the green histograms reveal the SN Deep limiting magnitudes to be on average between 0.6 and 1.2 mag deeper in the shallow fields, and 1.7–2.1 mag deeper in the deep fields. In the *z*-band, the difference is closer to 2 mag in the shallow fields and 3 mag in the deep fields, demonstrating the relative enhancement at redder wavelengths.

---

[5]The deblending procedure is explained in detail in the unofficial SExtractor manual http://astroa.physics.metu.edu.tr/MANUALS/sextractor/Guide2source_extractor.png
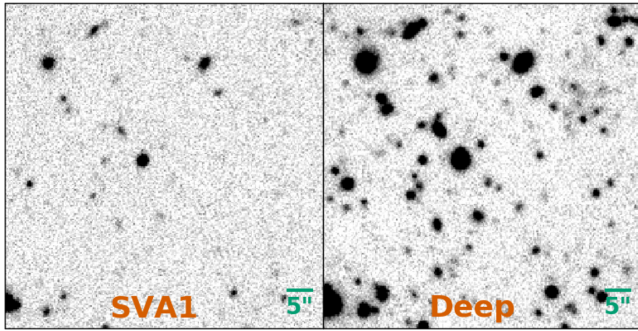[6]https://des.ncsa.illinois.edu/releases/sva1

**Figure 6.** A comparison between the *r*-band coadds from SVA1 (the previous coadds used for DES-SN host analysis; left), and this work (right), for a small region of the C3 field. The addition of detail on brighter objects as well as the detection of fainter objects is clearly visible.
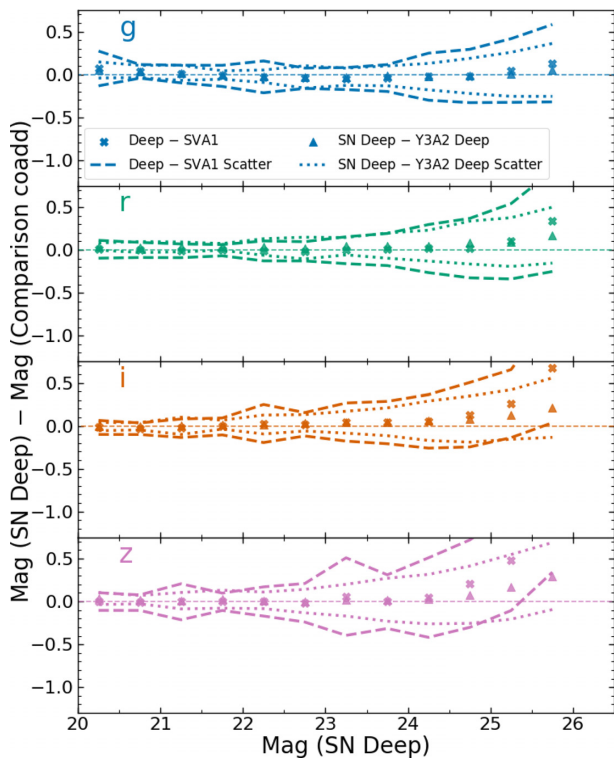


**Figure 7.** The difference in magnitude between the SN Deep coadd (this work) and two comparison catalogues: the SVA1 coadd and the Y3A2 Deep coadd. Shown here are the differences for objects that lie in the X2 field, binned by their brightness. The dashed and dotted lines trace the scatter in the magnitude differences for each comparison, respectively. In general, the data are centred around a magnitude difference of 0, indicating that the photometry is consistent.

To assess the quality of the deep photometry, we compare our photometry to previous DES catalogues of the SN fields. In this section, results will be listed corresponding to the *g*, *r*, *i*, and *z* bands, respectively. In Fig. 7, we plot the residual between the magnitudes from a subset of objects in a single CCD of our deep catalogues and the same matched objects in SVA1 as well as a set of deep coadds using a different processing pipeline, known as Y3A2_DEEP (DES Collaboration in preparation). The offsets between SN Deep and the two comparison catalogues are small, with the absolute mean differences to Y3A2_Deep at 0.05 mag or smaller. There is a general
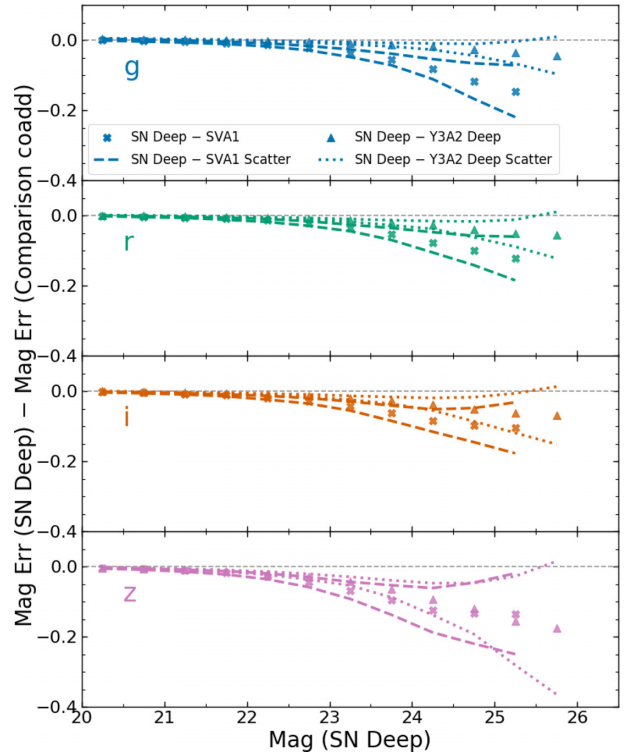


**Figure 8.** As per Fig. 7, but comparing the differences in magnitude errors (Mag Err). The increasingly negative tail at fainter magnitudes implies more precisely measured values in SN Deep.

trend towards a positive offset at the fainter (i.e. $>25$) mag, with SN Deep reporting around 0.1 mag fainter than Y3A2_Deep (the comparison to SVA1 at $m > 25$ is uninformative, as it is beyond the typical depth of that catalogue). The scatter in the differences, traced by the dashed lines, increases with magnitude. The scatter is smaller for the comparison to Y3A2_Deep than for SVA1, reinforcing the assumption that magnitudes reported in the deeper catalogues are closer to the 'truth' values.

Fig. 8 shows the difference in the magnitude uncertainties (MAGERR_AUTO) between the same matched galaxies. In addition to the statistical uncertainty, we also include the zero-point uncertainty in our final magnitude uncertainties. The uncertainty reported from SVA1 is systematically larger than the combined SN Deep uncertainty, and the difference increases at fainter magnitudes. This trend also exists in the comparison with Y3A2_Deep, although the strength is band-dependent, with more improvement noticeable with increasing wavelength.

## 2.5 Host matching

To remain consistent with the DES-SN3YR method (D'Andrea et al. 2018), we match transients to host galaxies in SN Deep using the directional light radius (DLR) method (Sullivan et al. 2006; Gupta et al. 2016). The matching algorithm chooses the host with the smallest $d_{DLR}$, which is the ratio between angular separation between the transient and the centre of a galaxy, and the size of that galaxy in the direction of the transient. As with D'Andrea et al. (2018), we use a threshold of $d_{DLR} \leq 4$; any object with no galaxies within this threshold is determined to be hostless.

### 2.5.1 Changes from SVA1

In total, of the 31 473 transient candidates in DES-SN, 24 695 (78.5 per cent) have an assigned host galaxy in the SVA1 catalogue. Using the deep coadds, that number is increased to 27 548 (87.5 per cent). Of the transients with SVA1 hosts, 23 943 (97 per cent) have the same host in SN Deep, with 280 objects (i.e. 1.1 per cent of those that already had a host) changing to a different host. A further 3325 (10.6 per cent of all transients) have a host in SN Deep that was not the host in SVA1; for 547 (1.7 per cent of all transients) of these, the SN Deep host was listed in the SVA1 catalogue but had $d_{DLR} > 4$ and thus was not considered the host. 26 objects move the other way – that is, their SVA1 host is the best match in SN Deep, but is now $d_{DLR} > 4$. Finally, there are 446 (1.4 per cent) transients that had a host in SVA1 but that galaxy is not detected in SN Deep. These objects are located in the gaps between CCDs in the deep coadds, a problem which was avoided in SVA1 by tiling observations. For these objects, we use the SVA1 data in the SN Deep catalogue. For the spectroscopically confirmed sample of SNe Ia used in the DES3YR analysis, the use of SN Deep means 13 SNe Ia (6.3 per cent) are assigned a host when they did not have one in SVA1, while 4 objects (2 per cent) are assigned a different host. One object lies on a chip gap and thus is not covered by SN Deep. A comparison of the behaviour of the SN Ia host galaxy mass step with the use of this photometry versus that from SVA1 can be found in Smith et al. (2020, hereafter S20).

As a further measure of the increased depth of the deep coadds, we calculated the apparent magnitude distributions of the assigned hosts of all DES transients using the DLR method in both SVA1 and SN Deep, and show the results in Fig. 9. The difference between the two distributions are shown beneath for each band. The shape (negative at bright magnitudes, positive at faint magnitudes) is caused by transients whose assigned host has changed from a brighter galaxy in SVA1 to a fainter galaxy in SN Deep. The transition appears roughly consistent with $g = 24.5$, and at increasingly brighter magnitudes through the longer wavelengths, which corresponding to the evolution of the magnitude limit of SVA1. A thorough exploration of how host mismatching may affect cosmological studies will be presented in a future paper following the technique of Popovic, Scolnic & Kessler (2020).

## 3 HOST SED MODELLING

In this section, we estimate stellar masses for the host galaxies of various subsamples of DES-SN transients. The goal is to be able to compare the host stellar mass distribution of various classes of transients to those observed in other surveys. The DES and comparison samples are introduced in the respective sections below. The true power of the SN Deep catalogue will eventually lie in the analysis of host galaxies of large, photometrically selected transient samples from DES, which are to be presented in the near future and are beyond the scope of this paper. As such, here we use predominantly spectroscopically selected samples and choose a variety of literature samples with which to compare our data. We do so in a proof of concept fashion, to showcase both the precision in mass measurements made possible by the coadds, as well as to introduce a probabilistic method to compare samples.

### 3.1 Parameter estimation

In order to estimate stellar masses of the galaxies comprising the DES-SN host samples, we fit the *griz* SED of each host galaxy with
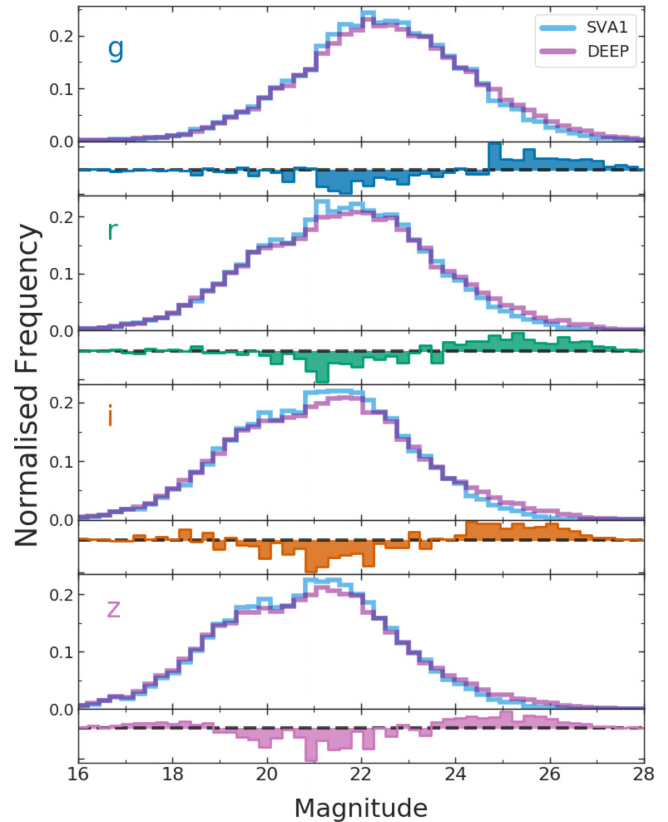


**Figure 9.** The normalized histograms of the magnitudes of SN host galaxies in the SVA1 (cyan) and the deep (purple) catalogues (upper panels), and deep − SVA1 (lower panels). At magnitudes where the difference is negative, a larger fraction of the SVA1 hosts lie at that magnitude than the corresponding fraction in the deep catalogue. Conversely, positive differences mean there are the fraction of deep hosts at that magnitude is greater than the fraction of SVA1 hosts. In all four bands, the distributions are skewed more strongly to fainter magnitudes.

templates formed of a combination of simple stellar population models. The fitting method, which makes use of the PÉGASE.2 spectral synthesis templates (Fioc & Rocca-Volmerange 1997; Le Borgne & Rocca-Volmerange 2002) and a Kroupa (2001) initial mass function (IMF), is described in S20. As per Palmese et al. (2020), we include a 0.1 dex systematic uncertainty on derived masses due to an apparent degeneracy between stellar mass and dust extinction.

### 3.2 Host galaxy samples

Below, we describe the host galaxy samples for which we calculate stellar masses. The SN selection and classifications used here are described primarily in D'Andrea et al. (2018).

The host galaxy samples are derived by matching each transient to galaxies detected in the deep coadds via the DLR method outlined in Section 2.5. To be included in the following analysis, the host galaxy must have an associated redshift, which can be taken from one of multiple sources. Most redshifts are derived from the dedicated DES spectral follow-up programme OzDES at the Anglo-Australian Telescope (AAT), and we take those with redshift flag 3 or 4 that correspond to good (∼95 per cent confidence) and excellent (a clear, unambiguous redshift) qualities, respectively (see Childress et al. 2017 for details on OzDES redshift flags). A minority of redshifts

come from other legacy redshift catalogues, or derived from the classification spectra of the SN itself. The requirement of having a spectroscopic redshift introduces various selection biases to the samples that are not well characterized. In detail, the selection function will depend not only on the brightness of the hosts but also on the strength of emission and absorption features in the host spectra (Yuan et al. 2015). An exploration of the implications of the host galaxy selection function will be presented in Möller et al. (in preparation).

Here, we describe the DES subsamples along with the selection of literature samples we use for comparison.

### 3.2.1 SNe Ia

We model the host galaxy SEDs for spectroscopically confirmed SNe Ia from the full five years of DES-SN. We include SNe Ia with DES classifications SNIa and SNIa? as defined in D'Andrea et al. (2018), which are the classifications used in the DES3YR cosmological analysis. Classifications were obtained with a number of different telescopes and instruments under different programmes, including one to specifically target SNe in faint host galaxies. In order to minimize host-galaxy selection bias, we include only SNe classified by the magnitude-limited OzDES live-transient follow-up programme (D'Andrea et al. 2018), and thus refer to the sample as DES SNe Ia (AAT). We further impose the restriction that the host galaxy must have a measured redshift. This redshift requirement means we exclude 'hostless' objects, thus likely biasing our sample to higher masses. This sample comprises 207 galaxies with mean redshift $\hat{z} = 0.30$.

We compare the DES (AAT) sample to the host galaxies of 82 SNe Ia in the local Universe from the Palomar Transient Factory (PTF; Pan et al. 2014) with $\hat{z} = 0.05$, as well as 279 at cosmological distances in the PanSTARRS 1 survey (PS1; Scolnic et al. 2018) with $\hat{z} = 0.29$ and 353 from the Supernova Legacy Survey (SNLS) using the sample of Roman et al. (2018) with $\hat{z} = 0.63$. The stellar masses in the above samples have all been measured using PÉGASE.2 templates. The PTF and PS1 samples were fit assuming a Salpeter (1955) IMF, whereas Roman et al. (2018) use a Rana & Basu (1992) IMF. Stellar masses derived with different IMF assumptions are known to lead to offsets in results. We scale the comparison samples by the factors prescribed in Speagle et al. (2014) in order to compare directly with our own mass estimates.

### 3.2.2 CCSNe

We include host galaxies of all SNe with the following spectroscopic classifications: SNIb/c/bc, II, IIb, IIn. Objects belonging to the SLSN subclasses are treated separately. For the same reasons as with the SNe Ia, we use subsample that was classified with the AAT, resulting in a sample of 47 objects. We compare the DES sample ($\hat{z} = 0.14$) to the subsample of CCSNe from Kelly & Kirshner (2012, hereafter KK12) that were discovered in untargeted surveys. This results in 117 objects with $\hat{z} = 0.04$. Host galaxy properties were measured from SDSS photometry, using PÉGASE.2 templates and a Rana & Basu (1992) IMF for the SED fitting.

### 3.2.3 SLSNe

We include host galaxies of all SLSNe from the sample of Angus et al. (2019) for which a galaxy is detected and a redshift is available. We relax the magnitude-limited selection criterion in

order to maintain the sample size. While this means that the sample is not homogeneously selected, we note that the comparison samples have been selected in a similar fashion. We compare the 22 DES SLSN sample to the SLSN samples of PTF (Perley et al. 2016c; 32 objects at $\hat{z} = 0.25$) who use a custom SED-fitting code using Bruzual & Charlot (2003) templates and a Chabrier (2003) IMF, and the combined Pan-STARRS and literature sample of Lunnan et al. (2014), which we denote PS + (31 objects, $\hat{z} = 0.64$), who use the FAST SED-fitting code (Kriek et al. 2009) with Maraston (2005) templates and a Salpeter (1955) IMF. We also compare to the DES CCSNe (AAT) sample. We note that two of the DES SLSNe (DES14X3taz and DES15X1noe) have light curves with detections in the season subsequent to discovery, meaning the galaxy photometry could be contaminated by SN light from that season. We compare the photometry for the host galaxy from the coadd with the main season removed with one where the season removed is neither of those in which the SN is bright. We find that the reported host magnitudes are consistent within measurement uncertainties, and thus do not affect our results substantially. We nevertheless flag these values in the corresponding results in Table B3.

### 3.2.4 RETs

Rapidly evolving transients (RETs) are bright events of unknown origin that rise and decline on much faster time-scales than classical SNe (Drout et al. 2014; Arcavi 2018; Pursiainen et al. 2018). We include hosts from the photometrically defined samples of Pursiainen et al. (2018) and Wiseman et al. (2020) for which a host is detected and a redshift is available. The final sample includes 51 objects. The DES RET sample is compared to the Gold and Silver samples from PS1 (Drout et al. 2014; 10 objects at $\hat{z} = 0.27$). PS1 stellar masses have been calculated in the same way as the PS+SLSNe. We also compare DES RETs to the DES CCSNe (AAT) and SNe Ia (AAT) samples.

## 4  HOST STELLAR MASS DISTRIBUTIONS

In this section, we construct cumulative distributions of host galaxy stellar masses, and statistically compare the DES samples to those from the literature that have been introduced in Section 3.2. The host galaxy magnitudes, redshifts, and derived stellar masses for each DES sample are reported in Tables B1–B4.

### 4.1 Probabilistic treatment of mass distributions

Here, we introduce the probabilistic methods used to estimate the true observed stellar mass distributions including upper limits, as well as a Bayesian method to compare the resulting distributions.

The probability density function (PDF) and cumulative density function (CDF) for the host stellar masses of the above-described samples are shown in Figs 10–13. The CDF represents the cumulative fraction of the total sample of hosts with a stellar mass at or below a given value. The shape of the CDFs of different samples can therefore be used as a comparison, and is often the basis of the 'two-sample' tests used to determine if the samples were drawn from the same parent population.

A difficulty arises when for some SNe no host galaxy is detected and only an upper limit is reported. The problem is that the host mass could take any value lower than the upper limit, and thus it is not known at what value the galaxy should be added to the
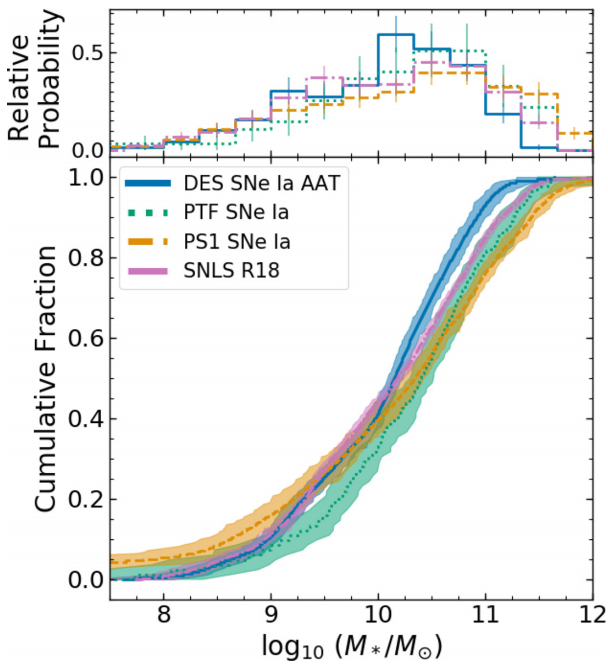
**Figure 10.** The cumulative distribution of the stellar masses of SNe Ia hosts in DES (this work & S20), PS1 (Scolnic et al. 2018), PTF (Pan et al. 2014), and SNLS (Roman et al. 2018). The CDF has been estimated using a Monte Carlo oriented technique similar to survival analysis. The shaded regions represent the $1\sigma$ uncertainties on the distribution (Section 4.2). DES separates from the other samples in the $10^{10}$–$10^{11}$ $M_\odot$ mass range.
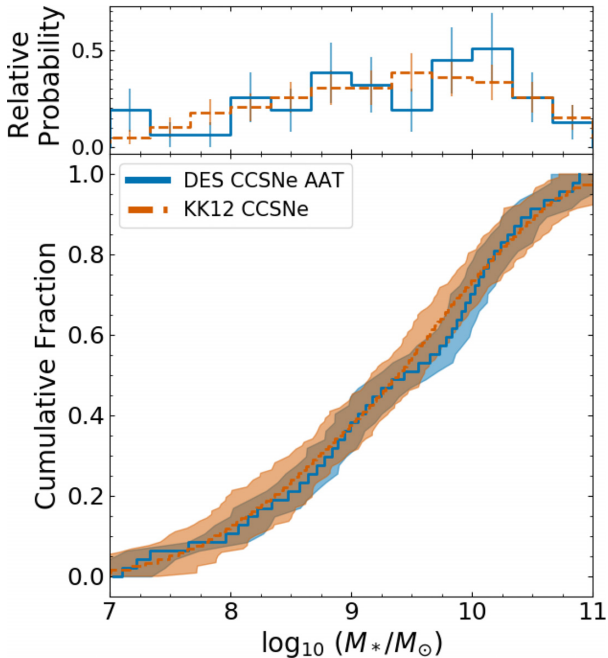
**Figure 12.** SLSN host stellar mass distributions from DES (this work & Angus et al. 2019), PTF (Perley et al. 2016a), PS+ (Lunnan et al. 2014), as well as DES CCSNe (this work). SLSNe hosts are systematically less massive than CCSNe. The DES sample is consistent with both literature samples.
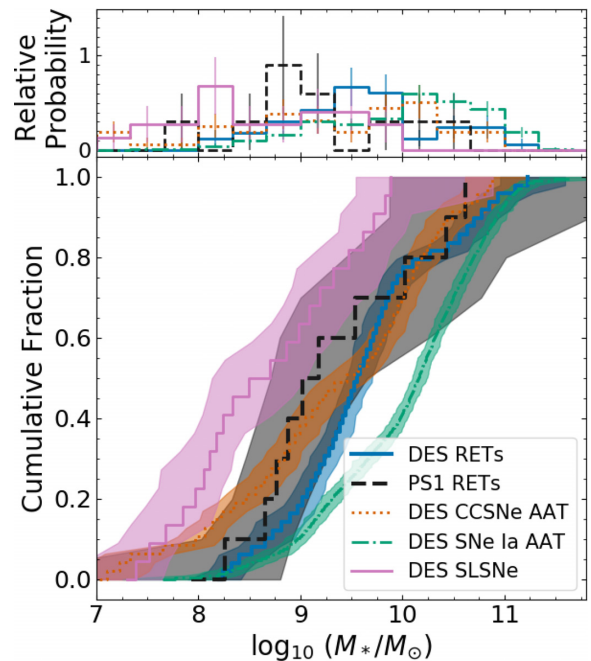
**Figure 11.** CCSNe host stellar mass distributions from DES (AAT) (this work) and KK12. The distributions appear consistent with one another.

**Figure 13.** RET host stellar mass distributions from DES (this work) and PS1 (Drout et al. 2014), as well as CCSNe, SNe Ia, and SLSNe from DES (this work).

CDF. Typically, to incorporate upper limits in estimating the CDF, astronomers use survival analysis, a technique developed principally for the assessment of the effectiveness of drugs in curing illness, with authors commonly using historical survival analysis packages such as ASURV[7] or the PYTHON package LIFELINES. Those packages are based around the Kaplan–Meier (KM) estimator (Kaplan & Meier 1958) of the survival function that approximates the most

[7] http://astrostatistics.psu.edu/statcodes/asurv

likely values for the non-detections based on the detected data, and inserts them into the CDF. However, this selection is only performed once, does not incorporate knowledge of the uncertainty on the objects that were detected, and assumes that the non-detections follow the same intrinsic magnitude distribution as the detected data.

To create our CDFs, we treat both detected points and upper limits as probability distributions. Detections are treated as Gaussians, with a mean and standard deviation corresponding to their detected values and uncertainties. Upper limits are treated as a skewed normal probability distribution, chosen such that the peak of the distribution is aligned with the upper limit minus the mean uncertainty on the detected galaxies. We use a distribution with a skew of $-7$, indicating the distribution is heavily skewed towards the lower end. This way, there is a small but finite probability of the true mass being higher than, but within uncertainty of, the given upper limit. We then simulate $10^4$ realizations of the CDF, each time randomly drawing from the given PDF for each observation. We then take the median, minimum and maximum mass values for each incremental increase in the fraction observed in order to construct the median CDF, and its lower and upper $1\sigma$ uncertainty. We find that this method reproduces the CDF given by KM estimation to a good degree, but we are more robust to noisy data having included measurement uncertainties.

To compare host stellar mass distributions, we follow the method described in Kruschke ([2013]). We model the PDF of each host sample as skewed-normal distributions. We adopt the SCIPY terminology: the skewed-normal distributions are parametrized by their 'loc' ($\mu$, analogous to the mean for a distribution with skewness 0), 'scale' ($\sigma$, analogous to the standard deviation for a distribution with skewness 0), and 'skewness' ($\alpha$, indicating the direction and strength of the skew of the distribution). We begin by assuming as a null hypothesis that both sample distributions are drawn from the same underlying population, and as such choose priors based on the combination of the samples. For $\mu$ we apply a normal prior, with the hyperparameters set as the mean and double the standard deviation of the combined sample. For $\sigma$ we apply a uniform prior between 0 and the range of masses in the combined sample. For $\alpha$, we apply a weak normal prior centred on $-3$ with a standard deviation of 5, since we expect host mass distributions to be negatively skewed as the rate of supernovae typically scales with stellar mass. A key advantage over traditional two-sample comparisons such as the Kolmogorov–Smirnov (KS) test is our inclusion of the uncertainty in the likelihood function. By incorporating this uncertainty, we are robustly handling the upper limits and poorly constrained observations so prevalent in observational astronomy. We sample from the posterior distribution using the PYMC3[8] package, using the No-U-Turn Sampler (NUTS; Hoffman & Gelman [2011]), which is initialized using `jitter + adapt_diag`. We sample with two walkers with a total of 10 000 iterations each after a warm-up stage of 5000 iterations. For each pair of samples, we then compare the estimates for $\mu$, $\sigma$, and $\alpha$ along with their resulting uncertainties. Since there are some degeneracies between the three parameters, and since they are not physically motivated, we do not calculate a confidence at which the samples are drawn from the same population (i.e. the KS $p$-value). Instead, we quote the probability that each parameter is the same for both samples, and comment on the physical implications. The best-fitting distributions and parameter confidence intervals can be found in Appendices C and D. The implications of the different host mass distributions for these sample are discussed in Section 5.2. We stress that these are

observed distributions; we do not correct for the numerous selection effects that likely affect each sample.

## 4.2 SNe Ia

For brevity, in the Results and Discussion sections we refer to the spectroscopic subsamples defined in Section 3.2 as DES. Unless otherwise stated, stellar masses are given in units of $\log_{10}(M_*/M_\odot)$. The mean (median) stellar mass of the DES sample is 10.01 (10.15). The average stellar masses from the PS1, PTF, and SNLS samples are similar, but all slightly higher mass than DES: PTF has a mean (median) of 10.25 (10.39); PS1 a mean (median) of 10.07 (10.32); SNLS a mean (median) of 10.08 (10.17). There is a clear difference between the PDFs of DES and the other surveys, with a sharp peak at $\sim$10.2 and a steeper high-mass decline. This manifests in the CDF as a steeper rise and hints at a preference for slightly lower mass galaxies, or that there is a smaller fraction of SNe in higher mass galaxies. PS1, on the other hand, has a shallower distribution.

The simultaneous fitting of the stellar mass distributions (see Appendix C for plots of the posterior samples) shows that the DES and PS1 hosts are clearly distinct. The mean difference in 'loc' parameter (which determines the location of the peak of the distribution, but does not correspond directly to the mean, median, or mode), $-0.28$, is nearly five times the standard deviation of the posterior distributions of the differences in loc (0.06). The mean difference in scale is $-0.4 \pm 0.09$, indicating the DES PDF is significantly narrower. The difference in skewness is less strongly constrained at $-2.4 \pm 2.6$, the stronger DES skewness resulting from the sharper high-mass cut-off. We thus find that the distributions, if assumed to be skewed-normal, are statistically different with the DES (AAT) sample lying at systematically lower $M_*$.

The comparison between DES and SNLS SNe Ia is very similar to that to PS1. While the shapes of the DES and SNLS distributions are more similar to each other than DES and PS1 (the difference between scales, and between skewnesses, is smaller), there is still an offset in loc of $-0.26$, significant at five times the standard deviation and are thus clearly derived from different observed populations.

The DES and PTF Ia host stellar mass distributions are more similar. The difference in their locs is much smaller than for the DES-PS1 comparison, and is only mildly significant ($0.12 \pm 0.06$), as the distributions peak at very similar masses. Similarly, the difference in the scale of the PDFs is small (0.18). PTF is thus marginally more strongly skewed, although the significance of this difference is negligible when the uncertainty is taken into account. On the whole we suggest these two distributions are very similar, while acknowledging minor differences between the DES and PTF distributions around the $1\sigma$ significance.

The SN Ia results and possible causes for differences between the surveys are discussed in Section 5.2.1.

We note here that stellar masses for the hosts of SNe Ia in the DES3YR analysis were estimated using photometry from the SVA1 catalogue. In S20, the stellar masses are re-evaluated using SN Deep photometry. The weighted mean stellar mass reduces from $10.64 \pm 0.06$ to $10.16 \pm 0.05$. A detailed investigation of the implications of the SN Deep catalogue for the SN Ia host galaxy mass step is presented in S20.

## 4.3 CCSNe

The PDFs and CDFs of CCSNe host masses are shown in Fig. [11]. The CCSNe samples systematically lie at lower mass than the SNe Ia. The DES mean (median) is 9.27 (9.39) while for KK12 this is

9.26 (9.39). The Bayesian fits to their PDFs appear similar, with DES shifted to slightly higher masses. The mean differences in loc is small (0.36 ± 0.09), while the scales are almost identical (a difference of −0.002 ± 0.094). The DES CCSNe hosts are far more skewed (−6.9 compared to −1.6). As with the DES and SNLS SNe Ia, the DES CCSNe mass distribution has a strong double-peaked nature, meaning the PDF is not well approximated by a single skewed-normal distribution. The fit in this case is driven by the peaks and is not hugely sensitive to the dip between masses of 9 and 10. Although the fits provide a suggestion that the two populations are different – we exercise caution and suggest that the double-peaked nature may be due to strong selection effects, which we discuss in Section 5.2.2.

### 4.4 SLSNe

The host galaxies of SLSNe are on average lower in stellar mass than those of CCSNe. The means (medians) of the DES, PTF, and PS+ samples being 8.67 (8.58), 8.75 (8.70), and 8.35 (8.19), respectively.

The skewed-normal fits to the SLSN samples are more loosely constrained than the SNe Ia and CCSNe due to their small sizes (22, 32, and 31 objects, respectively, many of which are upper limits), particularly for the DES sample. However, there are some notable differences. The SLSN sample CDFs all appear to follow a similar shape to each other, rising steeply rising at lower mass, while the CCSN sample is shallower and peaks at higher mass.

The DES SLSN host mass distribution is clearly shifted to higher values than the PTF and PS+ samples, with loc differences of 2.2 ± 0.36 and 1.5 ± 0.7, respectively. The DES sample displays a mild negative skew, while the PTF and PS+ samples are positively skewed with the peaks of the distribution lying at much lower masses. On the other hand, the DES SLSNe reside in lower mass galaxies compared to the DES CCSNe, with a difference in loc of −1.1 ± 0.4. Based on these findings, we conclude that the DES SLSN host galaxy is statistically different to the PS+ and PTF samples as well as the DES CCSN sample. The strong differences seen between SLSN samples are likely driven by selection effects, and are discussed in Section 5.2.3.

### 4.5 RETs

The mean (median) RET host mass is 9.59 (9.41) for DES and 9.20 (9.04) for PS1. This is significantly larger than the SLSN samples, and consistent with the CCSNe. Rapid transient hosts do not appear to follow the CDFs of SNe Ia, CCSNe, or SLSNe. There is a plateau in the DES RETs CDF around $\log_{10}(M_*/M_\odot) = 10$ which bears resemblance to the PTF SLSNe CDF. However, the RET hosts CDF rises again, with around 20 per cent of the galaxies lying above 10.5.

A simple skewed-normal distribution does not fit the PS1 RET PDF particularly well due to the sample size of only 10 objects. Inspecting the CDF shows that the DES and PS1 RET host mass distributions are consistent within errors, particularly at the high-mass end, although the PS1 sample is has a higher proportion of objects at lower mass.

The DES RET PDF is most similar to the SLSNe. There are still strong differences: the RETs are located at higher mass, although the difference is not significant (difference in loc 0.11 ± 0.45). The RET host distribution is consistent with zero skewness (0.54 ± 0.93), compared to the negatively skewed SLSNe. The differences between the DES RETs and the CCSNe and SNe Ia are significantly

stronger, with the RETs lying at lower mass by −1.28 ± 0.30 and −1.76 ± 0.31, respectively, with the RET distribution also being narrower in both cases. While they occur on average in lower mass hosts than SNe Ia and CCSNe, the the DES RET hosts appear to be significantly higher in mass than the DES SLSNe, although given that the skewed-normal fit to the DES SLSN PDF is largely unconstrained we do not claim that they are statistically different.

We thus conclude that the DES RET host mass sample is significantly different to the DES samples of SLSNe, CCSNe, and SNe Ia.

## 5 DISCUSSION

### 5.1 Coadds

We have created a set of deep images in order to obtain precise and accurate measurements of DES supernova host galaxies, a subset of which are presented in a catalogue here. We have optimized the coadds almost entirely for depth, without focussing much attention on the resulting PSF, nor on the removal of the faintest of artefacts. For that reason, these coadds are not optimal for studies such as weak lensing or those which require accurate modelling of galaxy morphology and light profiles. For those studies, we refer the reader to DES Collaboration (in preparation). However, Figs 6–9 are clear evidence for success of the depth-optimized coadds – we detect fainter hosts, thus improving the fraction of correctly assigned hosts. We also reduce the error compared to the shallower SV catalogues as well the deep catalogue that has not used a depth optimization.

To our knowledge, we thus present the highest volume host galaxy catalogue for an untargeted transient survey, which will allow a thorough exploration of host magnitude and mass distributions, misidentification fraction and spectroscopic/photometric redshift efficiency, to be presented in future work along with the DES-SN 5YR cosmological analysis.

A further advantage of our work is the ease with which the selection of input images can be optimized for desired characteristics in the resulting coadd. We refer the reader to Kelsey (in preparation), who optimize the stacks for resultant seeing.

### 5.2 Host stellar masses

#### 5.2.1 SNe Ia

The results presented in Section 4.2 show the host galaxy stellar masses of the DES SNe Ia (AAT) sample to be significantly different from that of the PS1 and SNLS samples, consistent with the conclusion derived by S20 using the KS test. The shape is more similar to that of the PTF sample.

DES SNe Ia (AAT) hosts lie, on the whole, at lower mass, with a tendency to avoid galaxies above $\log_{10}(M_*/M_\odot) \sim 11.5$. One reason for this could be the selection criteria for the DES sample. All SNe included in this sample were classified using the AAT, a 4m telescope using a fibre-fed spectrograph. It is likely that the spectra of some of the SNe that occurred in higher mass galaxies are dominated by relatively bright host galaxy continuum, hindering a classification. The 5 yr, photometrically selected sample should be devoid of these effects. On the other hand, the lack of inclusion of hostless objects and those missing a host-galaxy redshift in this sample is likely to have added a bias in the other direction: that is, apparently hostless SNe must have exploded in a region
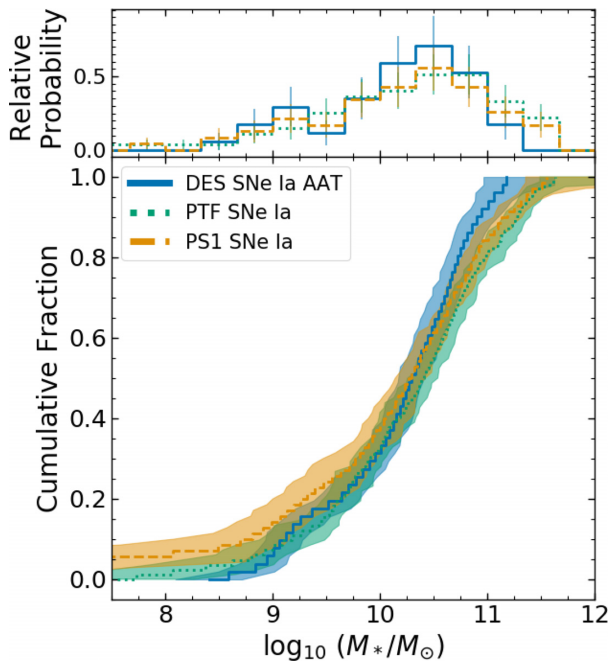
**Figure 14.** As per Fig. 10 but restricted to $z < 0.2$. The distributions are much more consistent with each other, suggesting that the samples are complete and robust against selection effects at low redshift.
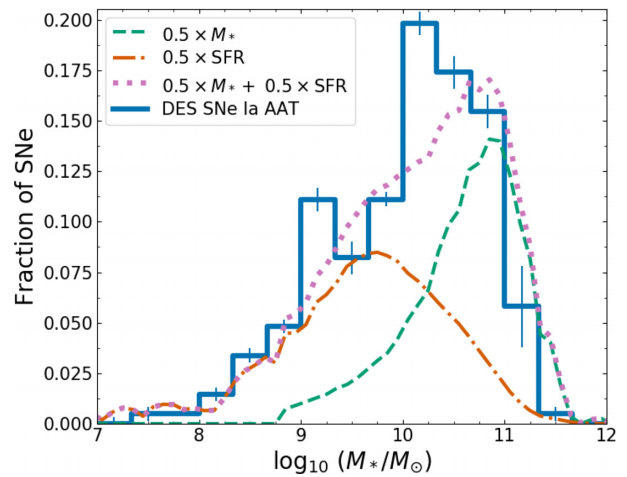


**Figure 15.** The DES SNe Ia (AAT) host stellar mass distribution as shown in Fig. 10 (blue, solid line) compared to the relative distribution of stellar mass ($M_*$, based on the $K$-band survey of Beare et al. 2019) and the distribution of star formation rate (SFR) in terms of the stellar mass of star-forming galaxies from SDSS (Abazajian et al. 2009). $M_*$ and SFR have been scaled by 0.5 such that their sum is 1.

of low stellar mass for no host to have been detected. A future analysis will develop on the survival analysis developed here in order to include objects with no redshift, while the effects of the host galaxy selection function will be explored in Möller et al. (in preparation).

The differences between the distributions could be caused in part by the selection function at different redshifts. To test this, we restricted the redshifts to $z < 0.2$. The resulting CDF is shown in Fig. 14 and shows that the DES, PS1, and PTF samples are broadly consistent at low-$z$. The divergence in the full CDFs is therefore attributable to the high-$z$ selection function, which is a combination of the SN detection and classification efficiencies (which are dependent on host galaxy mass), as well as the host galaxy detection completeness and redshift measurement completeness.

SNe Ia are thought to arise in various types of stellar population: the young, 'prompt' SNe Ia, associated with young stellar populations and thus in star-forming galaxies; and the older, 'delayed' population, which occur in old stellar populations (e.g. Scannapieco & Bildsten 2005; Sullivan et al. 2006, 2010; Childress et al. 2014), and thus are found in both star-forming and passive galaxies. The shape of the host galaxy mass distribution at a given redshift is thus expected to be shaped by a combination of the mass-distribution of the SFR and the raw stellar-mass distribution, and the relative contributions of these two distributions can help constrain the distribution of SN Ia progenitors among stellar populations. As per Childress et al. (2013a, 2013b), in Fig. 15 we show the DES SNe Ia host stellar mass PDF compared to a sum of the stellar mass distribution of SFR from SDSS Data Release 7 (Abazajian et al. 2009), and to the raw stellar mass distribution as measured by near-infrared photometry (Beare et al. 2019). We cut the samples to the appropriate redshift range to match the DES SN Ia sample. We scale the SFR and raw $M_*$ distributions by half, such that when summed their distributions approximate the total SN Ia host

mass distribution. The SN Ia host mass distribution resembles this combination well. The location of the subpeak at $\log_{10}(M_*/M_\odot) \sim 9$ is in the regime where the SN Ia rate is dominated by star formation rather than stellar mass, the so-called prompt population. We do not perform a fit of the host mass function to the SFR plus stellar mass combination, but an analysis with the full 5 yr, photometrically selected DES-SN data set will be presented in future work.

### 5.2.2 CCSNe

The DES and KK12 CCSNe host mass distributions are mildly different from one another based on the Bayesian fitting of a skewed-normal distribution, with the DES sample weighted to slightly higher masses than that from Kelly & Kirshner (2012). However, visual inspection shows the DES sample to be double-peaked, with an apparent lack of hosts with masses of $\log_{10}(M_*/M_\odot) \sim 9.5-10$. This may be a by-product of the selection function, as CCSNe are in general fainter than SNe Ia, as well as having fewer strongly distinguishing features, such that they are even more difficult to classify when the spectrum is dominated by a massive host galaxy. However, this would be more apparent as a high-mass cut-off rather than a double peak. We anticipate that a larger, photometrically selected DES CCSNe sample with smaller selection effects will be able to clarify the nature of this distribution, and will present that analysis in a future work.

CCSNe occur in regions of ongoing star formation, and thus the stellar masses of their host galaxies are expected to trace the mass distribution of star-forming galaxies, without the higher mass contribution from the raw stellar mass that is apparent in the SN Ia host distribution. In Fig 16, we plot the CCSN host mass distribution compared to the mass distribution of star formation. The location of the peaks is roughly consistent around $\log_{10}(M_*/M_\odot) = 10$, while the maximum CCSN host mass is consistent with the upper galaxy mass at which there is significant star formation, suggesting there is no obvious other factor (such as metallicity) inhibiting the production of CCSNe, which we might see if we had split the samples up into subtypes.
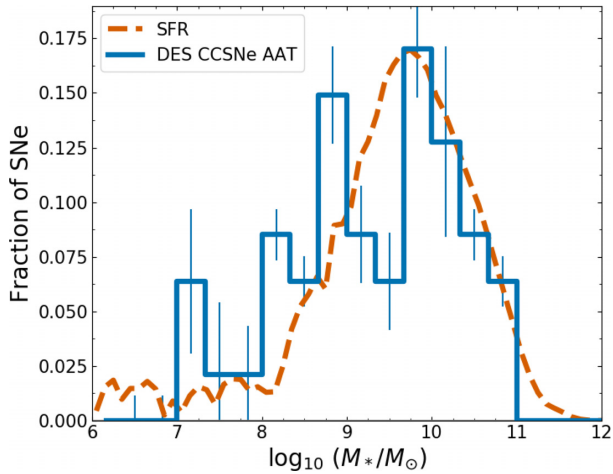
**Figure 16.** The DES CCSNe (AAT) host stellar mass distribution as shown in Fig. 11, compared to the relative mass distribution of star formation from SDSS. The CCSNe appear to trace the mass distribution of the SFR.



**Figure 17.** The DES RET and SLSN host stellar mass distributions as shown in Figs 12 and 13, compared to the relative mass distribution of star formation from SDSS. The SLSN distribution is distinct from the SFR, but the distinction for RETs is not so clear.

### 5.2.3 SLSNe

SLSNe show a strong preference for low-mass, low-metallicity, highly star-forming host galaxies (e.g. Lunnan et al. 2014; Leloudas et al. 2015; Angus et al. 2016; Chen et al. 2016). We have shown in Fig. 12 and Section 4.4 that for stellar mass, the same is true for the DES sample. This result is reinforced by Fig. 17, where the SLSN host mass PDF has a cut-off at much lower masses than the SFR distribution. The host masses are higher than the PS+ and PTF samples, which could be related to the DES SLSNe themselves showing strong light curve and spectral diversity, extending to fainter luminosities than the PS+ sample in particular, and covering a broader redshift range (Angus et al. 2019). Recently, a handful of SLSNe have been discovered in high-mass hosts (Chen et al. 2017b; Izzo et al. 2017); future large, volume limited complete samples from the Zwicky Transient Facility (ZTF) and the Large Synoptic Sky Survey (LSST) will be able to determine whether these high-mass hosts are statistical anomalies, or whether previous and current studies were biased strongly by selection criteria.

### 5.2.4 RETs

The DES sample of RETs is the largest to date by an order of magnitude. The hosts in the sample analysed here appear to have a stellar mass distribution unlike either SNe Ia, CCSNe, or SLSNe. They do not appear to trace the mass distribution of SFR (Fig. 17), although they follow it more closely than SLSNe, particularly at lower masses. It is unclear how the atypical shape of the distribution, in particular the lack of hosts at $\log_{10}(M_*/M_\odot) = 10$, could be caused by a selection effect. Typically selection biases have a smooth effect on the PDF, rather than the strong cut-off seen in the RET sample. There is a possibility that the effect is physical, such as the RETs belonging to more than one population of transients. In this scenario, a dominant population of transients could follow the SFR at low masses, but be subject to a metallicity threshold, while a subdominant population trace instead stellar mass and lead to the high-mass tail. This is certainly plausible, as the light-curve shapes and luminosities of the RETs show strong diversity (Pursiainen et al. 2018). A comprehensive analysis of the host galaxies of DES RETs can be found in Wiseman et al. (2020).
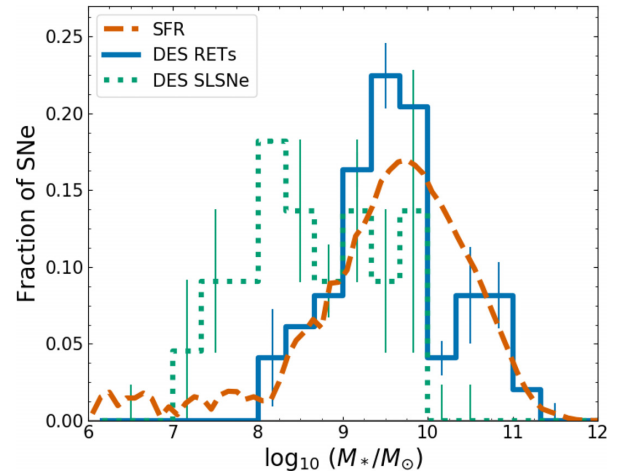
## 6 CONCLUSIONS

In this work, we have created a set of coadded optical images in the fields of the DES-SN programme, optimized for their ultimate depth. Simultaneously, we have created a framework with which it is possible to stack while optimizing for diagnostics of choice, such as seeing. With photometry reaching depths in excess of 27th magnitude, these coadds provide the basis for the ongoing analysis of the SN Ia host galaxy mass step in the DES3YR cosmological data set (S20; Kelsey in preparation), and lay the foundation for the full, photometrically selected analysis, currently in progress. Along with the direct use in the cosmological fit, these coadds and the derived galaxy catalogues provide room for exploration into further correlations between SN properties and their host galaxies.

The secondary outcome of this work is the comparison between the host masses of various samples of DES supernovae, and their corresponding samples from other surveys. By employing Monte Carlo-based techniques, we have allowed for the inclusion of uncertainties and limits in the construction of cumulative distributions. We further analyse by creating a probabilistic framework with which to then compare distributions while taking into account the uncertainties derived in their construction. We use this framework to infer that the DES type Ia supernova host galaxy stellar mass distribution is different to that from PS1 and SNLS, and more similar in shape to the PTF sample. The core-collapse supernova host galaxy sample is statistically similar to a low redshift compilation. We are unable to determine the degree to which these similarities and differences are inherent to the underlying host galaxy populations, or to the various selection biases associated with spectroscopically selected samples. The DES superluminous supernova hosts are similar in stellar mass to the PS+ and PTF samples, while the RET hosts are somewhat different to all of the other samples analysed, hinting at the possibility of multiple underlying transient and/or host galaxy populations.

Adding significant ancillary benefits to the project, deep colour images created from the DES-SN coadds have been used at public engagement events across the UK showcasing the importance and impact of surveys such as DES.

## REFERENCES

Abazajian K. N. et al., 2009, ApJS, 182, 543
Adelman-McCarthy J. K. et al., 2007, ApJS, 172, 634
Anderson J. P., Covarrubias R. A., James P. A., Hamuy M., Habergham S. M., 2010, MNRAS, 407, 2660
Angus C. R., Levan A. J., Perley D. A., Tanvir N. R., Lyman J. D., Stanway E. R., Fruchter A. S., 2016, MNRAS, 458, 84
Angus C. R. et al., 2019, MNRAS, 487, 2215
Annis J. et al., 2014, ApJ, 794, 120
Arcavi I., 2018, ApJ, 855, L23
Arcavi I. et al., 2014, ApJ, 793, 38
Astier P. et al., 2006, A&A, 447, 31
Beare R., Brown M. J. I., Pimblet K., Taylor E. N., 2019, ApJ, 873, 78
Bertin E., Arnouts S., 1996, A&AS, 117, 393
Bertin E., Mellier Y., Radovich M., Missonnier G., Didelon P., Morin B., 2002, in Bohlender D. A., Durand D., Handley T. H., eds, ASP Conf. Ser. Vol. 281, Astronomical Data Analysis Software and Systems XI. Astron. Soc. Pac., San Francisco, p. 228
Betoule M. et al., 2014, A&A, 568, A22
Bonnett C. et al., 2016, Phys. Rev. D, 94, 042005
Brout D. et al., 2019a, ApJ, 874, 106
Brout D. et al., 2019b, ApJ, 874, 150
Bruzual G., Charlot S., 2003, MNRAS, 344, 1000
Chabrier G., 2003, PASP, 115, 763
Chang C. et al., 2015, ApJ, 801, 73
Chen T. W., Smartt S. J., Yates R. M., Nicholl M., Krühler T., Schady P., Dennefeld M., Inserra C., 2016, MNRAS, 470, 3566
Chen T.-W. et al., 2017a, A&A, 602, A9
Chen T.-W. et al., 2017b, ApJ, 849, L4
Childress M. et al., 2013a, ApJ, 770, 107
Childress M. et al., 2013b, ApJ, 770, 108
Childress M. J., Wolf C., Zahid H. J., 2014, MNRAS, 445, 1898
Childress M. J. et al., 2017, MNRAS, 472, 273
Conley A. et al., 2011, ApJS, 192, 1
Contreras C. et al., 2018, ApJ, 859, 24
DES Collaboration, 2018, Phys. Rev. Lett., 122, 171301
Diehl H. T. et al., 2016, in Peck A. B., Seaman R. L., Benn C. R., eds, Proc. SPIE Vol. 9910, Observatory Operations: Strategies, Processes, and Systems VI. SPIE, Bellingham, p. 99101D
Diehl H. T. et al., 2018, in Peck A. B., Seaman R. L., Benn C. R., eds, Proc. SPIE Vol. 10704, Observatory Operations: Strategies, Processes, and Systems VII. SPIE, Bellingham, p. 107040D
Drout M. R. et al., 2014, ApJ, 794, 23
D'Andrea C. B. et al., 2018, preprint (arXiv:1811.09565)
Fioc M., Rocca-Volmerange B., 1997, A&A, 326, 950
Flaugher B. et al., 2015, ApJ, 150, 150
French K. D., Arcavi I., Zabludoff A., 2016, ApJ, 818, L21
Fruchter A. S. et al., 2006, Nature, 441, 463
Galbany L. et al., 2018, ApJ, 855, 107

Graham J. F., Fruchter A. S., 2017, ApJ, 834, 170
Gruen D., Seitz S., Bernstein G. M., 2014a, PASP, 126, 158
Gruen D. et al., 2014b, MNRAS, 442, 1507
Gupta R. R. et al., 2016, ApJ, 152, 154
Hoffman M. D., Gelman A., 2011, J. Mach. Learn. Res., 15, 1593
Izzo L. et al., 2017, A&A, 610, A11
Japelj J., Vergani S. D., Salvaterra R., Renzo M., Zapartas E., de Mink S. E., Kaper L., Zibetti S., 2018, A&A, 617, A105
Jarvis M. et al., 2016, MNRAS, 460, 2245
Jones D. O. et al., 2018, ApJ, 867, 108
Kaplan E. L., Meier P., 1958, J. Am. Stat. Assoc., 53, 457
Kelly P. L., Kirshner R. P., 2012, ApJ, 759, 107
Kelly P. L., Hicken M., Burke D. L., Mandel K. S., Kirshner R. P., 2010, ApJ, 715, 743
Kessler R. et al., 2009, ApJS, 185, 32
Kessler R. et al., 2015, ApJ, 150, 172
Kessler R. et al., 2019, MNRAS, 485, 1171
Kriek M., Van Dokkum P. G., Labbé I., Franx M., Illingworth G. D., Marchesini D., Quadri R. F., 2009, ApJ, 700, 221
Kroupa P., 2001, MNRAS, 322, 231
Kruschke J. K., 2013, J. Exp. Psychol. Gen., 142, 573
Krühler T., Kuncarayakti H., Schady P., Anderson J. P., Galbany L., Gensior J., 2017a, A&A, 602, A85
Krühler T. et al., 2017b, A&A, 610, A14
Lampeitl H. et al., 2010, ApJ, 722, 566
Lasker J. et al., 2019, MNRAS, 485, 5329
Le Borgne D., Rocca-Volmerange B., 2002, A&A, 386, 446
Leloudas G. et al., 2009, A&A, 505, 265
Leloudas G. et al., 2015, MNRAS, 449, 917
Lidman C. et al., 2020, MNRAS, preprint (arXiv:2006.00449)
Lunnan R. et al., 2014, ApJ, 787, 138
Macaulay E. et al., 2019, MNRAS, 486, 2184
Maraston C., 2005, MNRAS, 362, 799
Melchior P. et al., 2015, MNRAS, 449, 2219
Modjaz M. et al., 2020, ApJ, 892, 153
Mohr J. J. et al., 2012, in Radziwill N. M., Chiozzi G., eds, Proc. SPIE Vol. 8451, Software and Cyberinfrastructure for Astronomy II. SPIE, Bellingham, p.84510D
Morganson E. et al., 2018, PASP, 130, 074501
Muthukrishna D., Narayan G., Mandel K. S., Biswas R., Hložek R., 2019, PASP, 131, 118002
Möller A., de Boissière T., 2019, MNRAS, 491, 4277
Neill J. D. et al., 2011, ApJ, 727, 15
Neilsen E., Annis J. T., Diehl H. T., Swanson M. E., D'Andrea C., Kent S., Drlica-Wagner A., 2019, FERMILAB-TM-2714-AE-CD-PPD
Neilsen E., Bernstein G., Gruendl R., Kent S., 2016, FERMILAB-TM-2610-AE-CD
Oke J. B., Gunn J. E., 1983, ApJ, 266, 713
Oliver S. et al., 2000, MNRAS, 316, 749
Olmstead M. D. et al., 2014, ApJ, 147, 75
Palmese A. et al., 2017, ApJ, 849, L34
Palmese A. et al., 2020, MNRAS, 493, 4591
Pan Y.-C. et al., 2014, MNRAS, 438, 1391

Perley D. A. et al., 2016a, ApJ, 817, 7
Perley D. A. et al., 2016b, ApJ, 817, 8
Perley D. A. et al., 2016c, ApJ, 830, 13
Perlmutter S. et al., 1999, ApJ, 517, 565
Pierre M. et al., 2004, J. Cosmol. Astropart. Phys., 2004, 171
Planck Collaboration, 2016, A&A, 594, A13
Popovic B., Scolnic D., Kessler R., 2020, ApJ, 890, 172
Pursiainen M. et al., 2018, MNRAS, 481, 894
Rana N., Basu S., 1992, A&A, 265, 499
Rest A. et al., 2014, ApJ, 795, 44
Riess A. G. et al., 1998, ApJ, 116, 1009
Rigault M. et al., 2013, A&A, 560, A66
Rigault M. et al., 2018, preprint (arXiv:1806.03849)
Roman M. et al., 2018, A&A, 615, A68
Rose B. M., Garnavich P. M., Berg M. A., 2019, ApJ, 874, 32
Rykoff E. S. et al., 2016, ApJS, 224, 1
Sako M. et al., 2008, ApJ, 135, 348
Sako M. et al., 2014, PASP, 130, 064002
Salpeter E. E., 1955, ApJ, 121, 161
Scannapieco E., Bildsten L., 2005, ApJ, 629, L85
Schady P., Eldridge J. J., Anderson J., Chen T.-W., Galbany L., Kuncarayakti H., Xiao L., 2019, MNRAS, 490, 4515
Scolnic D. M. et al., 2018, ApJ, 859, 101
Smith M. et al., 2020, MNRAS, 494, 4426 (S20)
Speagle J. S., Steinhardt C. L., Capak P. L., Silverman J. D., 2014, ApJS, 214, 15
Sullivan M. et al., 2006, ApJ, 648, 868
Sullivan M. et al., 2010, MNRAS, 406, 782
Suzuki N. et al., 2012, ApJ, 746, 85
Thöne C. C., Christensen L., Prochaska J. X., Bloom J. S., Gorosabel J., Fynbo J. P. U., Jakobsson P., Fruchter A. S., 2014, MNRAS, 441, 2034
Wiseman P. et al. 2020, MNRAS, preprint (arxiv:2005.08653)
Xue Y. Q. et al., 2011, ApJS, 195, 10
Yuan F. et al., 2015, MNRAS, 452, 3047

## SUPPORTING INFORMATION

Supplementary data are available at *MNRAS* online.

**Table A1.** Overview of the deep coadds.
**Table B1.** Host galaxy properties for the DES SN Ia sample.
**Table B2.** Host galaxy properties for the DES CCSN sample.
**Table B3.** Host galaxy properties for the DES SLSN sample.
**Table B4.** Host galaxy properties for the DES RET sample.

Please note: Oxford University Press is not responsible for the content or functionality of any supporting materials supplied by the authors. Any queries (other than missing material) should be directed to the corresponding author for the article.

## APPENDIX A: COADDS SUMMARY

See Table A1.

**Table A1.** Overview of the deep coadds. $N_{exp}$ is the number of single exposures in the coadd; $t_{exp; tot}$ is the total exposure time in hours; $m_{lim}$ is the limiting magnitude determined from the sky background. The full table is available online.

| Field | Band | MY | $\tau_{Cut}$ | PSF cut | $N_{exp}$ | $t_{exp; tot}$ | $m_{lim}$ |
|-------|------|----|----|---------|------|----------|-----------|
| SN-E1 | $g$ | 1 | 0.26 | 2.4 | 70 | 3.4 | 26.249 |
| SN-E1 | $g$ | 2 | 0.26 | 2.4 | 48 | 2.33 | 26.124 |
| SN-E1 | $g$ | 3 | 0.26 | 2.4 | 54 | 2.62 | 26.222 |
| SN-E1 | $g$ | 4 | 0.26 | 2.4 | 52 | 2.53 | 26.137 |
| SN-E1 | $g$ | 5 | 0.26 | 2.4 | 60 | 2.92 | 26.214 |

**Table B1.** Host galaxy properties for the DES SN Ia sample. Magnitudes are given in the observer frame and are not corrected for host galaxy extinction. The full table can be accessed in the online version of this manuscript.

| Name | $z$ | $g$ | $g$_err | $r$ | $r$_err | $i$ | $i$_err | $z$ | $z$_err | $M$ | M_err |
|------|-----|-----|---------|-----|---------|-----|---------|-----|---------|-----|-------|
| DES13E1ao | 0.17 | 22.84 | 0.02 | 22.32 | 0.01 | 22.18 | 0.02 | 22.08 | 0.02 | 8.41 | 0.02 |
| DES13C3dgs | 0.35 | 21.80 | 0.00 | 21.04 | 0.00 | 20.81 | 0.00 | 20.59 | 0.00 | 9.57 | 0.01 |
| DES13S1qv | 0.18 | 22.17 | 0.01 | 21.60 | 0.01 | 21.37 | 0.01 | 21.25 | 0.01 | 8.79 | 0.05 |
| DES13C1juw | 0.20 | 22.18 | 0.01 | 21.13 | 0.00 | 20.68 | 0.01 | 20.53 | 0.01 | 9.43 | 0.02 |
| DES13X3woy | 0.32 | 20.23 | 0.00 | 18.75 | 0.00 | 18.16 | 0.00 | 17.98 | 0.00 | 11.16 | 0.02 |

**Table B2.** Host galaxy properties for the DES CCSN sample. Magnitudes are given in the observer frame and are not corrected for host galaxy extinction. The full table can be accessed in the online version of this manuscript.

| Name | $z$ | $g$ | $g$_err | $r$ | $r$_err | $i$ | $i$_err | $z$ | $z$_err | $M$ | M_err |
|------|-----|-----|---------|-----|---------|-----|---------|-----|---------|-----|-------|
| DES13C3ui | 0.07 | 20.80 | 0.00 | 20.54 | 0.00 | 20.42 | 0.00 | 20.35 | 0.01 | 8.22 | 0.01 |
| DES13C1feu | 0.06 | 16.30 | 0.00 | 15.61 | 0.00 | 15.42 | 0.00 | 15.24 | 0.00 | 10.29 | 0.01 |
| DES13X3fca | 0.10 | 17.70 | 0.00 | 17.00 | 0.00 | 16.76 | 0.00 | 16.74 | 0.00 | 10.07 | 0.02 |
| DES15C3bj | 0.29 | 20.80 | 0.00 | 20.07 | 0.00 | 19.72 | 0.00 | 19.54 | 0.00 | 9.98 | 0.01 |
| DES15S1by | 0.13 | 20.18 | 0.00 | 19.72 | 0.00 | 19.50 | 0.00 | 19.36 | 0.00 | 9.23 | 0.05 |

# APPENDIX B: HOST GALAXY DATA

**Table B3.** Host galaxy properties for the DES SLSN sample. Magnitudes are given in the observer frame and are not corrected for host galaxy extinction. The full table can be accessed in the online version of this manuscript.

| Name | $z$ | $g$ | $g$_err | $r$ | $r$_err | $i$ | $i$_err | $z$ | $z$_err | $M$ | M_err |
|------|-----|-----|---------|-----|---------|-----|---------|-----|---------|-----|-------|
| DES13S2cmm | 0.66 | 24.12 | 0.06 | 23.44 | 0.04 | 22.99 | 0.03 | 23.20 | 0.06 | 8.86 | 0.09 |
| DES15S2nr | 0.22 | 23.82 | 0.05 | 23.51 | 0.05 | 23.26 | 0.05 | 23.01 | 0.06 | 8.05 | 0.06 |
| DES14E2slp | 0.51 | 23.63 | 0.04 | 22.62 | 0.02 | 22.32 | 0.02 | 22.06 | 0.03 | 9.36 | 0.04 |
| DES15S1nog | 0.57 | 23.43 | 0.03 | 22.67 | 0.02 | 22.33 | 0.02 | 22.21 | 0.02 | 9.24 | 0.02 |
| DES16C3dmp | 0.57 | 22.25 | 0.01 | 21.59 | 0.00 | 21.31 | 0.00 | 21.26 | 0.01 | 9.56 | 0.01 |

**Table B4.** Host galaxy properties for the DES RET sample. Magnitudes are given in the observer frame and are not corrected for host galaxy extinction. The full table can be accessed in the online version of this manuscript.

| Name | $z$ | $g$ | $g$_err | $r$ | $r$_err | $i$ | $i$_err | $z$ | $z$_err | $M$ | M_err |
|------|-----|-----|---------|-----|---------|-----|---------|-----|---------|-----|-------|
| DES13X3gms | 0.65 | 23.62 | 0.02 | 23.02 | 0.01 | 22.61 | 0.02 | 22.61 | 0.02 | 9.13 | 0.03 |
| DES13C1tgd | 0.20 | 21.28 | 0.00 | 20.31 | 0.00 | 19.75 | 0.00 | 19.59 | 0.00 | 9.90 | 0.01 |
| DES13S2wxf | 0.57 | 22.16 | 0.01 | 21.31 | 0.01 | 20.98 | 0.01 | 20.92 | 0.01 | 9.83 | 0.02 |
| DES13X1hav | 0.58 | 24.38 | 0.09 | 23.63 | 0.07 | 23.24 | 0.04 | 23.13 | 0.05 | 8.95 | 0.07 |
| DES13X3nyg | 0.71 | 23.84 | 0.03 | 23.39 | 0.02 | 22.96 | 0.02 | 22.92 | 0.03 | 9.06 | 0.03 |
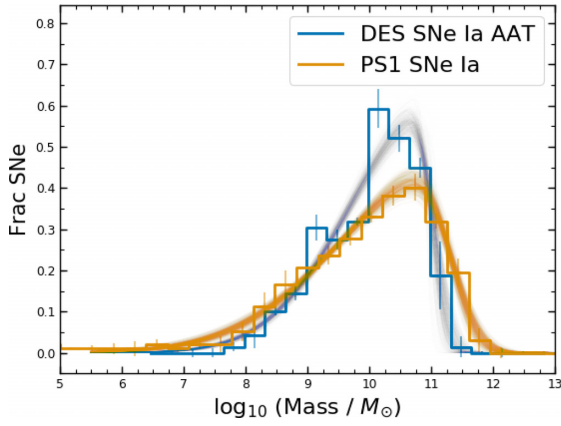
**Figure C1.** DES SNe Ia compared to PS1 SNe Ia.

## APPENDIX C: STELLAR MASS FITS

Here, we show the Bayesian fits that were used to compare between host stellar mass distributions as outlined in Section 4.1. The solid lines are taken from each of the MCMC samples. See Figs C1–C11.



**Figure C2.** DES SNe Ia compared to PTF SNe Ia.



**Figure C3.** DES SNe Ia compared to SNLS SNe Ia.



**Figure C4.** DES CCSNe compared to KK12 CCSNe.



**Figure C5.** DES SLSNe compared to DES CCSNe.
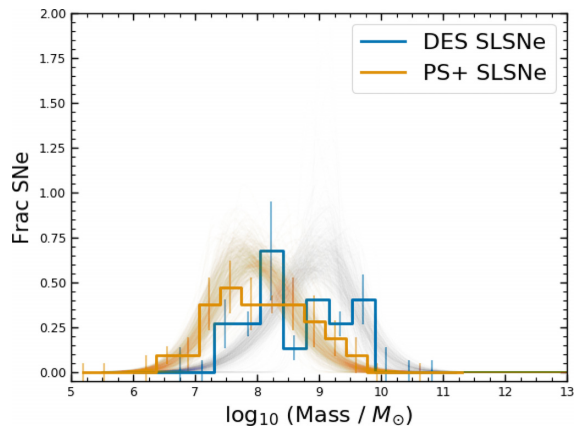


**Figure C6.** DES SLSNe compared to PS+SLSNe.
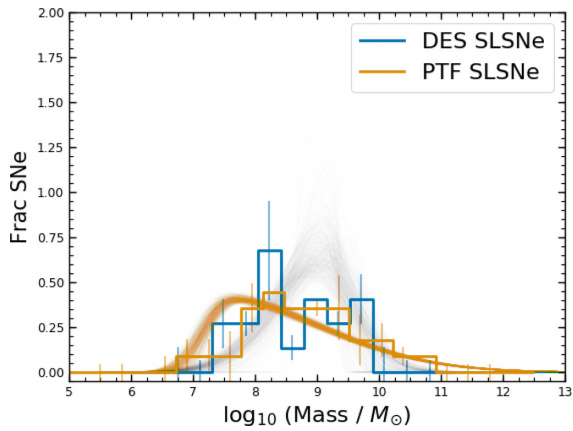
**Figure C7.** DES SLSNe compared to PTF SLSNe.
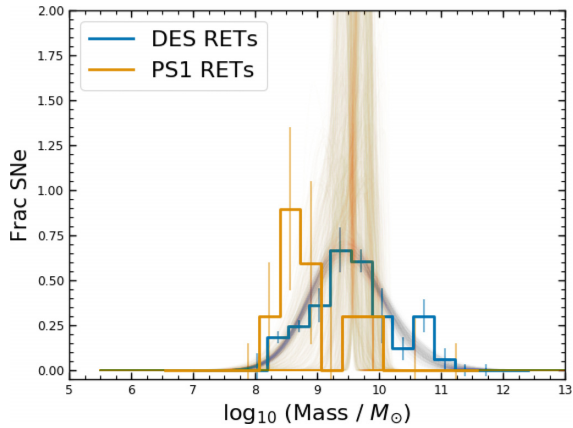
**Figure C8.** DES RETs compared to PS1 RETs classified.
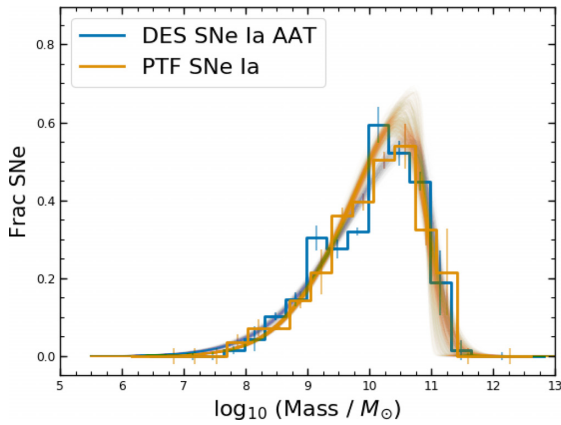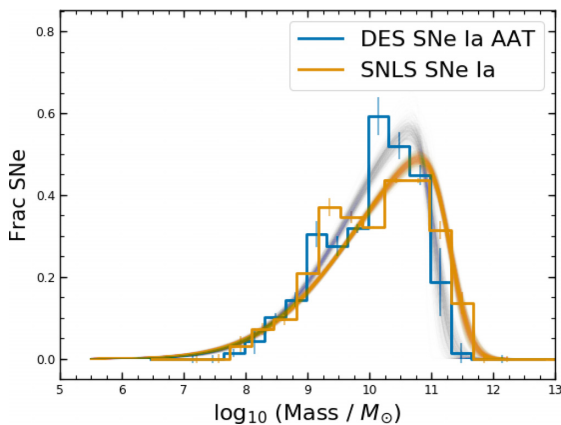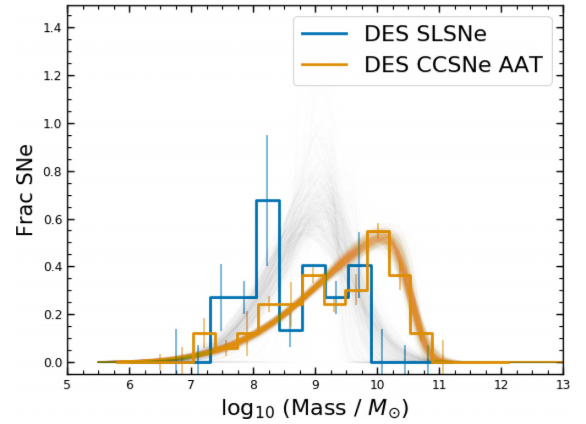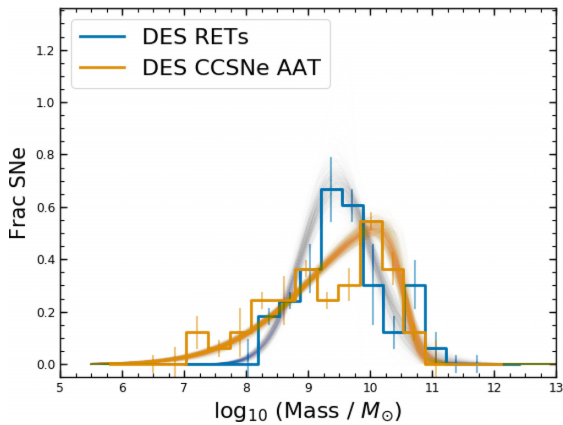
**Figure C9.** DES RETs compared to DES CCSNe.
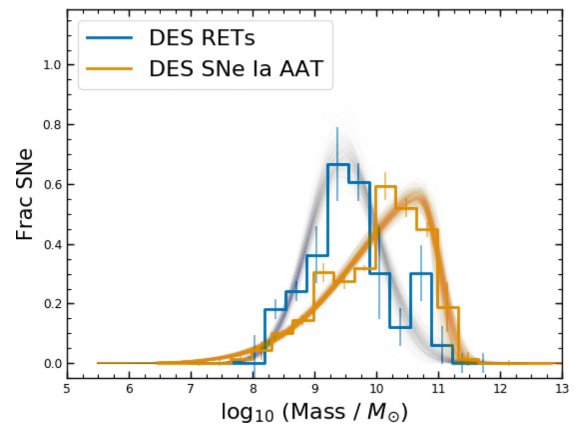
**Figure C10.** DES RETs compared to DES SNe Ia classified by OzDES.
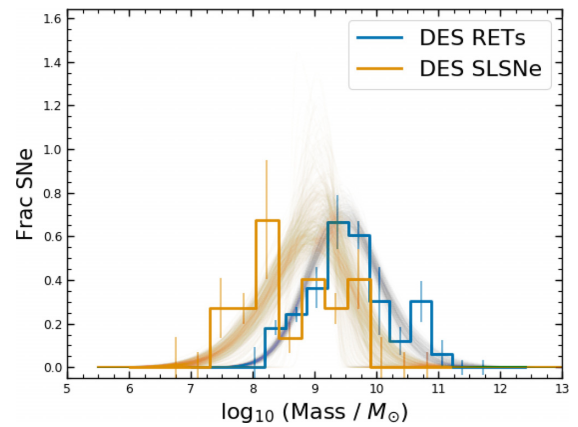
**Figure C11.** DES RETs compared to DES SLSNe.

## APPENDIX D: STELLAR MASS FIT PARAMETERS

The following tables show the results from the two-sample Bayesian fits as described in Section 4.1. Loc, scale, and alpha correspond to the location (i.e. central mass), width, and skewness of the distributions, respectively. Negative values in the difference parameters mean the DES sample (blue in Appendix C) has a lower value than the comparison sample (yellow in Appendix C). The columns mean, std, and mc_error correspond to the inferred mean and standard deviation of the posterior distribution, and the simulation standard error from the MCMC, respectively. See Tables D1–D4.

Downloaded from https://academic.oup.com/mnras/article-abstract/495/4/4040/5840549 by University College London user on 31 July 2020

**Table D1.** Results of the MCMC fits for comparing the stellar mass distributions for SNe Ia.

|  | Mean | std | mc_error |
|---|---|---|---|
| DES SNe Ia AAT loc | 11.047 | 0.050 | 0.000 |
| DES SNe Ia AAT scale | 1.343 | 0.043 | 0.000 |
| DES SNe Ia AAT alpha | −7.640 | 2.552 | 0.035 |
| PTF SNe Ia loc | 10.930 | 0.036 | 0.000 |
| PTF SNe Ia scale | 1.158 | 0.024 | 0.000 |
| PTF SNe Ia alpha | −5.621 | 3.286 | 0.069 |
| Difference of locs | 0.116 | 0.061 | 0.001 |
| Difference of scales | 0.184 | 0.049 | 0.001 |
| Difference of alphas | −2.019 | 4.158 | 0.083 |
| DES SNe Ia AAT loc | 11.048 | 0.050 | 0.001 |
| DES SNe Ia AAT scale | 1.344 | 0.042 | 0.000 |
| DES SNe Ia AAT alpha | −7.569 | 2.485 | 0.036 |
| PS1 SNe Ia loc | 11.327 | 0.040 | 0.000 |
| PS1 SNe Ia scale | 1.748 | 0.078 | 0.001 |
| PS1 SNe Ia alpha | −5.165 | 0.868 | 0.008 |
| Difference of locs | −0.278 | 0.064 | 0.001 |
| Difference of scales | −0.404 | 0.089 | 0.001 |
| Difference of alphas | −2.404 | 2.622 | 0.038 |
| DES SNe Ia AAT loc | 11.047 | 0.049 | 0.000 |
| DES SNe Ia AAT scale | 1.343 | 0.041 | 0.000 |
| DES SNe Ia AAT alpha | −7.585 | 2.546 | 0.032 |
| SNLS SNe Ia loc | 11.311 | 0.026 | 0.000 |
| SNLS SNe Ia scale | 1.506 | 0.035 | 0.000 |
| SNLS SNe Ia alpha | −5.817 | 0.637 | 0.006 |
| Difference of locs | −0.264 | 0.056 | 0.001 |
| Difference of scales | −0.163 | 0.055 | 0.001 |
| Difference of alphas | −1.769 | 2.613 | 0.033 |

**Table D2.** Results of the MCMC fits for comparing the stellar mass distributions for CCSNe.

|  | Mean | std | mc_error |
|---|---|---|---|
| DES CCSNe AAT loc | 10.539 | 0.049 | 0.001 |
| DES CCSNe AAT scale | 1.420 | 0.060 | 0.001 |
| DES CCSNe AAT alpha | −6.946 | 2.260 | 0.041 |
| KK12 CCSNe loc | 10.213 | 0.076 | 0.001 |
| KK12 CCSNe scale | 1.422 | 0.073 | 0.001 |
| KK12 CCSNe alpha | −1.621 | 0.294 | 0.005 |
| Difference of locs | 0.326 | 0.090 | 0.001 |
| Difference of scales | −0.002 | 0.094 | 0.001 |
| Difference of alphas | −5.325 | 2.277 | 0.041 |

**Table D3.** Results of the MCMC fits for comparing the stellar mass distributions for RETs.

|  | Mean | std | mc_error |
|---|---|---|---|
| DES RETs loc | 9.194 | 0.282 | 0.024 |
| DES RETs scale | 0.729 | 0.122 | 0.009 |
| DES RETs alpha | 0.837 | 0.864 | 0.072 |
| PS1 RETs loc | 9.698 | 0.238 | 0.017 |
| PS1 RETs scale | 0.330 | 0.216 | 0.015 |
| PS1 RETs alpha | −6.097 | 6.780 | 0.406 |
| Difference of locs | −0.504 | 0.354 | 0.027 |
| Difference of scales | 0.399 | 0.254 | 0.019 |
| Difference of alphas | 6.934 | 6.793 | 0.402 |
| DES RETs loc | 9.252 | 0.294 | 0.006 |
| DES RETs scale | 0.701 | 0.122 | 0.002 |
| DES RETs alpha | 0.639 | 0.965 | 0.021 |
| DES CCSNe AAT loc | 10.539 | 0.049 | 0.001 |

**Table D3** – *continued*

|  | Mean | std | mc_error |
|---|---|---|---|
| DES CCSNe AAT scale | 1.420 | 0.061 | 0.001 |
| DES CCSNe AAT alpha | −6.902 | 2.092 | 0.037 |
| Difference of locs | −1.286 | 0.299 | 0.006 |
| Difference of scales | −0.719 | 0.135 | 0.002 |
| Difference of alphas | 7.541 | 2.310 | 0.041 |
| DES RETs loc | 9.289 | 0.302 | 0.006 |
| DES RETs scale | 0.690 | 0.119 | 0.002 |
| DES RETs alpha | 0.537 | 0.933 | 0.019 |
| DES SNe Ia AAT loc | 11.048 | 0.049 | 0.001 |
| DES SNe Ia AAT scale | 1.343 | 0.042 | 0.000 |
| DES SNe Ia AAT alpha | −7.649 | 2.662 | 0.054 |
| Difference of locs | −1.759 | 0.306 | 0.006 |
| Difference of scales | −0.652 | 0.126 | 0.002 |
| Difference of alphas | 8.186 | 2.837 | 0.056 |
| DES RETs loc | 9.252 | 0.292 | 0.008 |
| DES RETs scale | 0.701 | 0.122 | 0.003 |
| DES RETs alpha | 0.649 | 0.908 | 0.025 |
| DES SLSNe loc | 9.364 | 0.337 | 0.009 |
| DES SLSNe scale | 0.865 | 0.146 | 0.003 |
| DES SLSNe alpha | −2.856 | 3.961 | 0.117 |
| Difference of locs | −0.112 | 0.453 | 0.013 |
| Difference of scales | −0.164 | 0.188 | 0.004 |
| Difference of alphas | 3.505 | 4.060 | 0.119 |

**Table D4.** Results of the MCMC fits for comparing the stellar mass distributions for SLSNe.

|  | Mean | std | mc_error |
|---|---|---|---|
| DES SLSNe loc | 9.348 | 0.353 | 0.014 |
| DES SLSNe scale | 0.862 | 0.146 | 0.004 |
| DES SLSNe alpha | −2.799 | 4.036 | 0.135 |
| PTF SLSNe loc | 7.153 | 0.082 | 0.001 |
| PTF SLSNe scale | 1.825 | 0.036 | 0.000 |
| PTF SLSNe alpha | 6.903 | 2.098 | 0.043 |
| Difference of locs | 2.195 | 0.362 | 0.014 |
| Difference of scales | −0.964 | 0.150 | 0.004 |
| Difference of alphas | −9.703 | 4.557 | 0.136 |
| DES SLSNe loc | 9.312 | 0.374 | 0.014 |
| DES SLSNe scale | 0.854 | 0.147 | 0.004 |
| DES SLSNe alpha | −2.487 | 3.829 | 0.141 |
| PS+SLSNe loc | 7.828 | 0.559 | 0.017 |
| PS+SLSNe scale | 0.793 | 0.130 | 0.002 |
| PS+SLSNe alpha | 0.571 | 3.059 | 0.104 |
| Difference of locs | 1.484 | 0.675 | 0.021 |
| Difference of scales | 0.060 | 0.198 | 0.005 |
| Difference of alphas | −3.059 | 4.847 | 0.163 |
| DES SLSNe loc | 9.349 | 0.351 | 0.011 |
| DES SLSNe scale | 0.860 | 0.147 | 0.003 |
| DES SLSNe alpha | −2.618 | 3.718 | 0.093 |
| DES CCSNe AAT loc | 10.539 | 0.050 | 0.001 |
| DES CCSNe AAT scale | 1.420 | 0.061 | 0.001 |
| DES CCSNe AAT alpha | −6.976 | 2.266 | 0.049 |
| Difference of locs | −1.189 | 0.355 | 0.011 |
| Difference of scales | −0.559 | 0.159 | 0.003 |
| Difference of alphas | 4.358 | 4.394 | 0.104 |

[1]*School of Physics and Astronomy, University of Southampton, Southampton SO17 1BJ, UK*
[2]*Université Clermont Auvergne, CNRS/IN2P3, LPC, F-63000 Clermont-Ferrand, France*
[3]*Lawrence Berkeley National Laboratory, 1 Cyclotron Road, Berkeley, CA 94720, USA*

[4]*Institute of Cosmology and Gravitation, University of Portsmouth, Portsmouth PO1 3FX, UK*

[5]*University of Copenhagen, Dark Cosmology Centre, Juliane Maries Vej 30, DK-2100 Copenhagen O, Denmark*

[6]*Department of Physics and Astronomy, University of Pennsylvania, Philadelphia, PA 19104, USA*

[7]*School of Mathematics and Physics, University of Queensland, Brisbane, QLD 4072, Australia*

[8]*Santa Cruz Institute for Particle Physics, Santa Cruz, CA 95064, USA*

[9]*PITT PACC, Department of Physics and Astronomy, University of Pittsburgh, Pittsburgh, PA 15260, USA*

[10]*School of Physics and Astronomy, Cardiff University, CF24 3AA, UK*

[11]*Department of Astronomy and Astrophysics, University of Chicago, Chicago, IL 60637, USA*

[12]*Kavli Institute for Cosmological Physics, University of Chicago, Chicago, IL 60637, USA*

[13]*Sydney Institute for Astronomy, School of Physics, A28, The University of Sydney, NSW 2006, Australia*

[14]*The Research School of Astronomy and Astrophysics, Australian National University, ACT 2601, Australia*

[15]*Department of Physics, Duke University Durham, NC 27708, USA*

[16]*Cerro Tololo Inter-American Observatory, National Optical Astronomy Observatory, Casilla 603, La Serena, Chile*

[17]*Departamento de Física Matemática, Instituto de Física, Universidade de São Paulo, CP 66318, São Paulo, SP 05314-970, Brazil*

[18]*Laboratório Interinstitucional de e-Astronomia - LIneA, Rua Gal. José Cristino 77, Rio de Janeiro, RJ - 20921-400, Brazil*

[19]*Fermi National Accelerator Laboratory, PO Box 500, Batavia, IL 60510, USA*

[20]*Instituto de Fisica Teorica UAM/CSIC, Universidad Autonoma de Madrid, E-28049 Madrid, Spain*

[21]*CNRS, UMR 7095, Institut d'Astrophysique de Paris, F-75014 Paris, France*

[22]*Sorbonne Universités, UPMC Univ Paris 06, UMR 7095, Institut d'Astrophysique de Paris, F-75014 Paris, France*

[23]*Department of Physics & Astronomy, University College London, Gower Street, London WC1E 6BT, UK*

[24]*Kavli Institute for Particle Astrophysics & Cosmology, PO Box 2450, Stanford University, Stanford CA 94305, USA*

[25]*SLAC National Accelerator Laboratory, Menlo Park, CA 94025, USA*

[26]*Centro de Investigaciones Energéticas, Medioambientales y Tecnológicas (CIEMAT), Av. Complutense 40, 28040, Madrid, Spain*

[27]*INAF, Astrophysical Observatory of Turin, I-10025 Pino Torinese, Italy*

[28]*Department of Astronomy, University of Illinois at Urbana-Champaign, 1002 W. Green Str, Urbana, IL 61801, USA*

[29]*National Center for Supercomputing Applications, 1205 West Clark Str, Urbana, IL 61801, USA*

[30]*Observatório Nacional, Rua Gal. José Cristino 77, Rio de Janeiro, RJ-20921-400, Brazil*

[31]*Department of Physics, IIT Hyderabad, Kandi, Telangana 502285, India*

[32]*Department of Astronomy/Steward Observatory, University of Arizona, 933 North Cherry Avenue, Tucson, AZ 85721-0065, USA*

[33]*Jet Propulsion Laboratory, California Institute of Technology, 4800 Oak Grove Dr., Pasadena, CA 91109, USA*

[34]*Institut d'Estudis Espacials de Catalunya (IEEC), E-08034 Barcelona, Spain*

[35]*Institute of Space Sciences (ICE, CSIC), Campus UAB, Carrer de Can Magrans, s/n, E-08193 Barcelona, Spain*

[36]*Department of Astronomy, University of Michigan, Ann Arbor, MI 48109, USA*

[37]*Department of Physics, University of Michigan, Ann Arbor, MI 48109, USA*

[38]*Centre for Astrophysics & Supercomputing, Swinburne University of Technology, Victoria 3122, Australia*

[39]*Département de Physique Théorique and Center for Astroparticle Physics, Université de Genève, 24 quai Ernest Ansermet, CH-1211 Geneva, Switzerland*

[40]*Department of Physics, ETH Zurich, Wolfgang-Pauli-Strasse 16, CH-8093 Zurich, Switzerland*

[41]*Center for Cosmology and Astro-Particle Physics, The Ohio State University, Columbus, OH 43210, USA*

[42]*Department of Physics, The Ohio State University, Columbus, OH 43210, USA*

[43]*Center for Astrophysics | Harvard & Smithsonian, 60 Garden Str, Cambridge, MA 02138, USA*

[44]*Australian Astronomical Optics, Macquarie University, North Ryde, NSW 2113, Australia*

[45]*Lowell Observatory, 1400 Mars Hill Rd, Flagstaff, AZ 86001, USA*

[46]*Department of Astronomy, The Ohio State University, Columbus, OH 43210, USA*

[47]*Department of Astrophysical Sciences, Princeton University, Peyton Hall, Princeton, NJ 08544, USA*

[48]*Institució Catalana de Recerca i Estudis Avançats, E-08010 Barcelona, Spain*

[49]*Institut de Física d'Altes Energies (IFAE), The Barcelona Institute of Science and Technology, Campus UAB, E-08193 Bellaterra (Barcelona), Spain*

[50]*Institute of Astronomy, University of Cambridge, Madingley Road, Cambridge CB3 0HA, UK*

[51]*Department of Physics and Astronomy, Pevensey Building, University of Sussex, Brighton BN1 9QH, UK*

[52]*Computer Science and Mathematics Division, Oak Ridge National Laboratory, Oak Ridge TN 37831, USA*

[53]*Max Planck Institute for Extraterrestrial Physics, Giessenbachstrasse, D-85748 Garching, Germany*

[54]*Universitäts-Sternwarte, Fakultät für Physik, Ludwig-Maximilians Universität München, Scheinerstr. 1, D-81679 München, Germany*

This paper has been typeset from a TEX/LATEX file prepared by the author.